

Convolutional Neural Network for Flow over Single and Tandem Elliptic Cylinders of Arbitrary Aspect Ratio and Angle of Attack

Shantanu Shahane^{a,1}, Purushotam Kumar^b, Surya Pratap Vanka^a

*a Department of Mechanical Science and Engineering,
University of Illinois at Urbana-Champaign, Urbana, Illinois 61801*

*b Manufacturing Technology & Engineering,
Corning Incorporated, Painted Post, NY, 14870*

Abstract

Machine learning is an emerging field of research in which complex data is compacted through low order models that can faithfully reproduce the original data with good accuracy. Machine learning of experimental and computational data sets of fluid mechanics is valuable for design optimization, sensitivity studies, fluid control, and as virtual laboratories in fluid mechanics education. In this study, we have developed convolutional neural network (CNN) models of two-dimensional laminar steady flow over single and tandem elliptic cylinders with various cylinder aspect ratios, angles of attack, cylinder separation, and flow Reynolds number. Multilayer perceptron neural networks (MLPNN) are used to estimate the lift and drag coefficients with the above parameters as input variables. The computational fluid dynamics data for training and validation of the neural networks is generated by the commercial software COMSOL using fine grids that gave grid-independent

¹Corresponding Author Email Address: shahaneshantanu@gmail.com

results. The paper presents development and application of the neural networks, sample demonstration at arbitrary sets of parameters, and sensitivity studies of the parametric effects on lift and drag coefficients. Line plots of the variations in lift and drag as functions of the governing parameters are also presented.

1. Introduction

The present study is concerned with the emerging discipline of Machine Learning (ML) [1–3] which seeks to explore physical phenomena through neural networks trained using data from experiments or numerical simulations. A typical study of machine learning consists of several initial numerical simulations or experiments with parameters chosen on a grid such as the Latin Hypercube [4, 5] spanning a multi-dimensional input space. The results of numerical simulations of the physical phenomena are then used to train a neural network with specified outputs. Once a neural network is trained and validated, it can then be used to quickly study characteristics of the phenomena in a multi-parameter space at low cost and optimize pre-determined objective functions. In comparison with actual full numerical simulations (or experiments), the neural networks execute much faster and can be coupled with techniques such as genetic algorithms and multi-objective optimization [6]. Neural networks can also be used to perform uncertainty quantification of flow and geometric parameters [7].

In the recent years, there has been growing interest in the coupling of various architectures such as recurrent (RNN), convolutional (CNN), multi-layer perceptron (MLPNN) neural networks with computational fluid dy-

namics and heat transfer. Takbiri-Borujeni et al. [8] developed a CNN based surrogate model for simulation of flow over porous media. They represented the domain with solid and void spaces using a binary image which is used as an input to the CNN with a U-ResNet architecture to estimate the flow field. Sun et al. [9] optimized the heat source layout on a circuit board with an objective to reduce the maximum temperature along the board. They used a deep neural network as a surrogate model of the inverse problem to map the temperature field to heat source layout, both represented as images. The neural network consists of convolutional layers with residual and long short term memory (LSTM) blocks. Han et al. [10] trained a convolutional LSTM network for prediction of unsteady flow over a cylinder and airfoil. The convolutional layers capture the spatial variations in the flow field whereas, the LSTM blocks learn the mapping between previous timesteps and a future timestep. Miyanawala and Jaiman [11] developed a CNN for unsteady flow over bluff bodies of varying topology including polygon, circle, ellipse and square with rounded edges. The input to the network is represented as a contour of the distance function based on the geometry of the bluff body. The network predicts time averaged force coefficients and vorticity. Rabault et al. [12] used reinforcement learning (RL) with CNN to develop an active flow control strategy for the Kármán vortex. Based on the mass flow rates of two jets on the sides of the cylinder, the network modifies the flow field to minimize the drag by perturbing the incoming mass flow rate. Bukka et al. [13] developed reduced order models using proper orthogonal decomposition (POD) and CNN to generate lower dimensional features. A recurrent network is further trained on these features. They considered unsteady flow over

single circular cylinder as well as side-by-side pair of cylinders. Ribeiro et al. [14] developed a CNN for steady laminar flow over bluff bodies of random shapes. The geometry of the bluff body is represented as a signed distance function. Sekar et al. [15] used a two step deep learning approach to model steady laminar flow over an airfoil. The first step consists of a CNN for extraction of geometrical parameters from an image of the airfoil. The second step estimates the velocity and pressure at various locations in the domain as a function of these parameters using MLPNN. Raissi and Karniadakis [16] used a physics informed neural network (PINN) to estimate parameters in the partial differential equations (PDE) such as viscosity and density based on scarcely sampled spatial and temporal variation of velocities. The basic idea behind PINN is to add the residual in the PDEs to the loss function of the neural network. They applied it to various problems including the Burgers' equation and unsteady flow over circular cylinder. Ogoke et al. [17] developed a graph based CNN (GCNN) to represent the flow field around airfoil over unstructured grids to estimate the drag force. GCNN encodes unstructured grid in the form of an adjacency matrix of the vertices and edges connecting them. Zhang et al. [18] optimized the lift and drag over an airfoil using an oscillating upstream cylinder. The amplitude and frequency of the oscillations as well as diameter of the cylinder and its distance from the airfoil are defined as the input process parameters in order to improve the lift and drag on the airfoil. They used the MLPNN to link these four process parameters to time averaged lift and drag coefficients. Jin et al. [19] developed a CNN for estimation of temporal snapshots of the velocity fields in the region around the cylinder as a function of the wall pressure coefficient

(C_p) on the cylinder. The C_p is represented as a two-dimensional image with x axis as non-dimensional time and y axis as the angle around the cylinder. Deng et al. [20] reconstructed the turbulent velocity field over single and side-by-side pair of cylinders from sparse experimental measurements. They used a generative adversarial network (GAN) with convolutional layers in order to improve the spatial resolution of the instantaneous flow fields and statistical flow quantities.

In this study, we apply the concept of convolutional and dense neural networks to study flow over single and tandem elliptic cylinders at various angles of attack, aspect ratios and inter-cylinder spacing. Flows behind bluff bodies placed in a uniform fluid stream have been studied extensively in fluid mechanics literature. Numerous research papers exist on canonical geometries of a circular cylinder [21–25], a square cylinder [26–30], and a flat plate [31–33]. Beginning with the early sketches by Da Vinci [34], the formation of a recirculation zone and the onset of unsteady shedding of vortices have been recognized as the distinct characteristics of flow behind an obstacle placed in a free stream. The alternate shedding of vortices from the shear layers due to the Kelvin–Helmholtz instability also gives rise to fluctuating lift and drag around the body caused by the alternating pressure forces around the body with a characteristic non-dimensional frequency called the Strouhal frequency. Numerous experimental, analytical, and numerical studies of flow over circular and rectangular cylinders have been previously reported. Computational studies ranging from very low Reynolds numbers to turbulent flows have been conducted for several canonical shapes using a variety of two-dimensional and three-dimensional numerical methods. Minimization

of drag of automobiles and tractor trailers while also considering stability issues has been extensively studied for propulsion systems.

Another canonical geometry that also possesses rich fluid physics and has practical relevance is an elliptical cylinder placed in a flowing fluid stream. The elliptical cylinder approaches the shapes of a flat plate for aspect ratio (ratio of maximum and minimum diameters, AR) of infinity, and a circular cylinder when AR is unity. Further, an elliptical cylinder can be placed at any arbitrary angular orientation with the free stream, providing another flow parameter in addition to aspect ratio and Reynolds number. Also, two or more elliptical cylinders can be placed in-line, or staggered, to passively control flow characteristics. Thus, elliptic cylinders provide a big parameter space to explore flow physics of fundamental and practical importance. Several studies have been conducted of wakes of elliptic cylinders but in comparison with those of circular and rectangular cylinders, such studies have been less in number.

Shintani et al. [35] analyzed the low Reynolds number flow past an elliptical cylinder placed normal to a uniform stream using a method of matched asymptotic expansions. Park et al. [36] numerically studied the flow past an impulsively started slender elliptic cylinder (aspect ratio of 14.89) for a Reynolds number between 25 and 600. The stream function vorticity transport equations are solved in an elliptical boundary-fitted coordinate system. The angle of incidence is varied at small increments of 2.5° between 0° and 90° at a fixed Reynolds number, and the flow regime is mapped. For small angles of attack, the flow is found to be steady up to Reynolds numbers of 300. Raman et al. [37] used a Cartesian grid code employing the immersed

boundary method to compute wake of an elliptic cylinder with aspect ratio varying between 0.1 and 1.0 in steps of 0.1. The wake formation and transition to unsteady flow are presented as a function of aspect ratio for a fixed Reynolds number. Paul et al. [38] followed the work of Raman et al. using the same numerical code and studied the effects of aspect ratio and angle of attack on wake characteristics of an elliptic cylinder. The different vortex shedding patterns are classified using the velocity and vorticity profiles. The lift, drag, and the Strouhal number are also documented as a function of the cylinder aspect ratio, angle of attack, and the Reynolds number.

Several studies of flow over impulsively started elliptic cylinders are also reported. Lugt and Haussling [39] computed the laminar flow over an abruptly accelerated cylinder at an angle of incidence of 45° . They observed steady flow only until $Re = 30$, and the von Kármán vortex shedding at $Re = 200$. Taneda [40] performed experiments of impulsively started elliptic cylinders and presented photographs of streak lines and streamlines. Patel [41] performed a semi-analytic study of an impulsively started elliptic cylinder at various angles of attack and presented flow patterns downstream of the cylinder. Ota et al. [42] also conducted experiments of flow around an elliptic cylinder and presented the Reynolds number for formation of a separation zone and for onset of vortex shedding. Nair and Sengupta [43] investigated high Reynolds number flow over an elliptical cylinder using a two-dimensional stream-function-vorticity formulation and third/fourth-order differencing of the convection terms. Effects of Reynolds number, angle of attack, and thickness to chord ratio are presented.

Faruquee et al. [44] studied the laminar flow over an elliptic cylinder in

the steady regime using the commercial CFD code FLUENT for a Reynolds number of 40 based on the hydraulic diameter. They varied the aspect ratio from 0.3 to 1 with the major axis oriented parallel to the free stream. They reported that no vortices are formed below an aspect ratio of 0.34, after which a pair of symmetric vortices are formed. The wake size and drag coefficient are observed to increase quadratically with the aspect ratio at the fixed Reynolds number of 40. Dennis and Young [45] studied the steady flow over an elliptic cylinder with minor to major axes ratios of 0.2 and 0.1 and for Reynolds number between 1 and 40. Lift and drag coefficients and surface vorticity distributions are presented for different angles of inclination. A series truncation method described by Badr et al. [46] is used. Jackson [28] used a finite element method to study laminar flow past cylinders of various shapes including elliptic cylinders. In this study, emphasis is based on the Hopf bifurcation from a steady flow to an unsteady flow as the Reynolds number is increased. The transition Reynolds number is estimated to vary from 35.7 at zero angle of attack to 141.4 at 90° for an ellipse of major to minor axis ratio of 2.0. D’alessio and Dennis [47] studied the steady flow over an elliptic cylinder at different angles of inclination using a stream–function–vorticity approach on a curvilinear grid for Reynolds number of 5 and 20. This study is followed by D’alessio et al. [48] in which the unsteady flow of an impulsively started elliptic cylinder translating about its axis is computed by the stream–function–vorticity approach. A similar study is also conducted by Patel [41].

In this study, we first conducted a large set of numerical simulations of flow over single and tandem elliptic cylinders [49] placed in a uniform free

stream. For a single cylinder, the aspect ratio defined as ratio of the major to minor axes is varied from 1 to 3, and the angle of inclination is varied counterclockwise from 0° to 180° degrees. For tandem inline cylinders, the aspect ratio and the angle of attack are varied independently for the two cylinders along with the separation. The ranges of aspect ratios, angles and separation are $[1, 3]$, $[0^\circ, 180^\circ]$ and $[4, 10]$ respectively. In addition, the free stream Reynolds number defined based on the free stream velocity and the major axis of the leading elliptical cylinder is varied in the range $[20, 40]$. The Reynolds number is limited to the steady regime and a convolutional neural network (CNN) is trained over a large data set spanning the three and six parameters for single and double cylinders respectively. The accuracy of the network is assessed on an unseen test data set and after ensuring acceptable accuracy, the network is applied to demonstrate the trends at different values of parameters. Since the neural network estimations run very fast, they can be performed interactively and can be used as virtual laboratories.

Section 2 briefly describes the commercial software COMSOL used to perform the initial CFD flow simulations. Section 3 describes the architectures and error analyses of the developed neural networks. Section 4 presents applications of the neural networks and demonstrates the observed trends in lift and drag coefficients as well as velocity and pressure contours as a function of input parameters. A summary and future directions is given in section 5.

2. Numerical Simulations of Flow over Elliptical Cylinders

To perform the flow computations, we have used the COMSOL software which solves the appropriate governing equations for the given set of flow

variables. COMSOL is a finite element based solver for multi-physics simulations. We have used the steady state two-dimensional laminar incompressible flow (spf) module. It solves the continuity and momentum equations in the x and y directions. An unstructured mesh with triangular elements has been used to discretize the domain. Quadratic elements with second order accurate discretization schemes are chosen to represent the velocity and pressure variables. The direct solver option with full velocity-pressure coupling is selected to solve for the flow field.

The minor axis of the ellipse is taken as one unit in length and the length of the major axis is varied as per the aspect ratio selected for the desired case. The computational domain has a length of 90 units and a height of 24 units. The distance of the flow inlet to the center of the upstream ellipse is 24 units, and the second ellipse is placed downstream with the specified separation. The six variables namely Reynolds number, two major to minor axis ratios, two angles of attack of the ellipses and the separation between center of ellipses are chosen as input parameters. The upstream velocity is fixed at 1 m/s and the kinematic viscosity is changed according to the Reynolds number. Reynolds number is defined with respect to the major axis of the upstream ellipse.

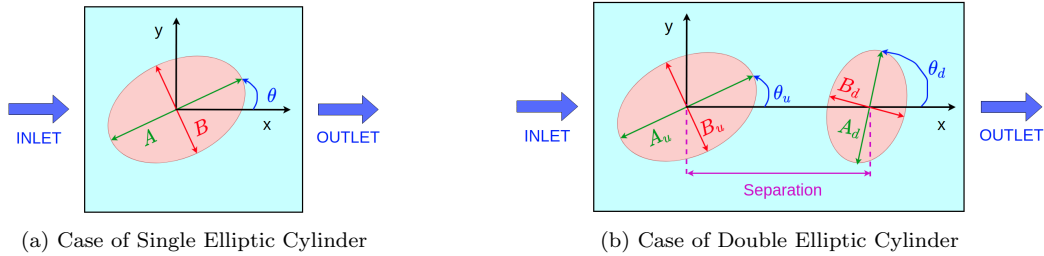


Figure 1: Schematic of the Flow Domain in the Vicinity of the Cylinders (Cylinder Dimensions Artificially Enlarged)

The top and bottom boundaries are specified to have the free stream velocities with no-slip conditions on the surfaces of the elliptic cylinders. Uniform unit normal and zero transverse velocities are prescribed at the inlet. Constant pressure is imposed at the outlet. The drag and lift coefficients are defined as

$$C_D = \frac{F_D}{0.5\rho U^2 A} \quad C_L = \frac{F_L}{0.5\rho U^2 A} \quad (1)$$

where, F_D and F_L are drag and lift forces per unit length respectively and A is taken to be the length of the major axis. Both pressure and viscous forces are included in calculation of drag and lift forces.

The computations are ensured to have low discretization errors by performing simulations on three different grids, as shown in figs. 2 and 3 for the region around cylinders. The finest grid is used in all the calculations in the following sections. Tables 1 and 2 give the computed lift and drag for the three grids to show the effects of grid refinement for both the single and double cylinder cases. The difference between the medium and finest grids is small, and the finest grid can be considered to give grid-independent results.

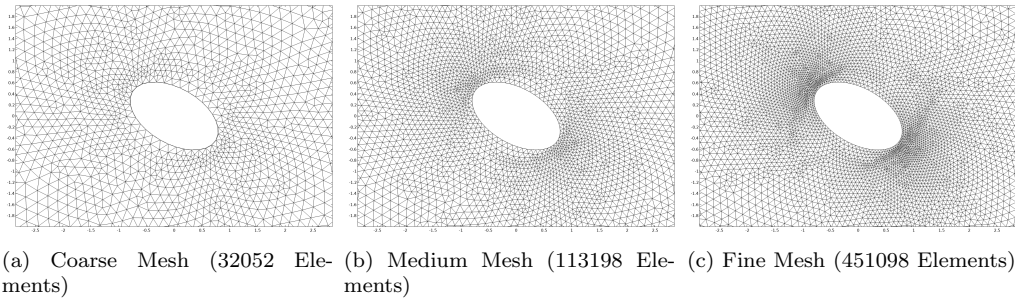


Figure 2: Single Cylinder Case: Successively Refined Meshes for Grid-Independence Study

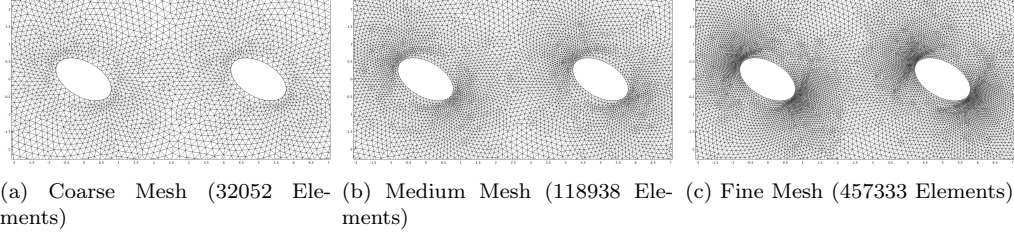


Figure 3: Double Cylinder Case: Successively Refined Meshes for Grid-Independence Study

	Lift	Drag
Coarse Mesh	0.3868	1.2160
Medium Mesh	0.3895	1.2289
Fine Mesh	0.3903	1.2306

Table 1: Single Cylinder Case: Lift and Drag Coefficients for 3 Refined Grids

	Lift Upstream	Drag Upstream	Lift Downstream	Drag Downstream
Coarse Mesh	0.3797	1.5202	0.1239	0.5510
Medium Mesh	0.3815	1.5341	0.1225	0.5550
Fine Mesh	0.3817	1.5358	0.1215	0.5560

Table 2: Double Cylinder Case: Lift and Drag Coefficients for 3 Refined Grids

3. Development of Neural Networks

We have used two different types of neural networks: multilayer perceptron (MLPNN) and convolutional neural network (CNN). Architectures and training processes of both the networks are described in this section.

3.1. Multilayer Perceptron Neural Network (MLPNN) for Prediction of Lift and Drag Coefficients

A perceptron, also known as neuron, is a building block of the network. A neuron performs linear transformation on the input vector followed by an element-wise nonlinear activation function to give an output. MLPNN is one of the simplest neural network architectures where neurons are stacked together to form a layer and multiple layers are combined to form a deep network. The linear transformation requires weights and biases which are estimated during the training process by minimizing the loss function. In this work, the mean squared error between estimates obtained from the numerical simulations and predictions of the neural network is defined as the loss function. Hyper-parameters such as number of layers, number of neurons, learning rate etc., are fine tuned by randomly splitting the data into two subsets: training and validation. We use 90% data for training and 10% for validation. A smaller network with few hidden neurons and layers does not fit the training data satisfactorily. This phenomenon is known as under-fitting or bias. Adding more neurons and layers increases the nonlinearity and thus, improves the prediction capability of the network. However, excessively deep networks tend to fit the training data with high accuracy but fail to generalize on unseen validation data. This is known as over-fitting or variance. In practice, a network with low bias and low variance is desired. This is achieved by using the validation data. The trained network is tested on an unseen dataset. A well trained network should perform satisfactorily on both training and testing sets i.e., it should demonstrate low errors and high accuracies on both the sets. More details of the network architecture,

training procedure, back-propagation algorithm etc. can be found in the literature [1]. In this work, we have used the open source Python library TensorFlow [50] with its high level API Keras [51].

Lift and drag coefficients are estimated as a function of Reynolds number and geometric parameters using the MLPNN architecture. For the case of a single elliptic cylinder, Reynolds number, angle of attack and ratio of major to minor axis are the three independent parameters which affect the lift and drag coefficients of the elliptic cylinder (fig. 4a). For the second case of double elliptic cylinder, the separation between them is an additional input parameter together with individual angles of attack and ratios (fig. 4b). The Reynolds number is defined with respect to the upstream elliptic cylinder. The Reynolds number, angle of attack, aspect ratio and separation are varied in the ranges $[10, 40]$, $[0^\circ, 180^\circ]$, $[1, 3]$ and $[4, 10]$ respectively. The range of Reynolds number is chosen such that a steady state solution exists for the lowest aspect ratio of unity. For a circular cylinder, the critical Reynolds number is around 42.

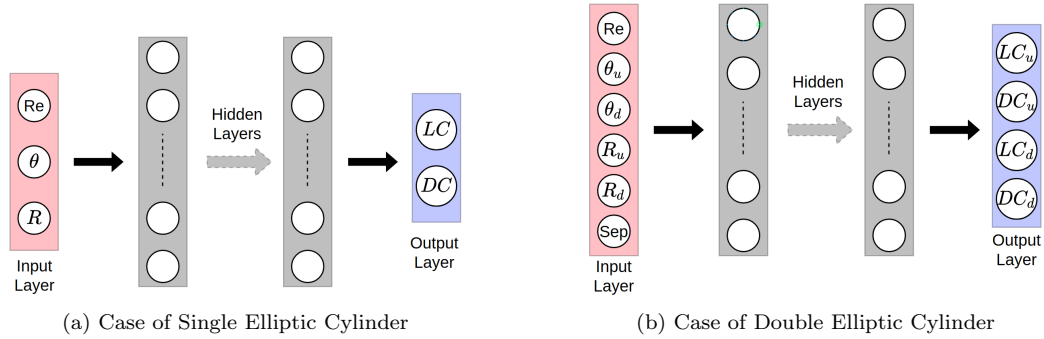


Figure 4: MLPNN for Estimation of Lift and Drag Coefficients (LC : lift coefficient, DC : drag coefficient, Re : Reynolds no., θ : angle of attack, R : ratio of major to minor axis, subscript u : upstream, subscript d : downstream)

	Case of Single Elliptic Cylinder	Case of Double Elliptic Cylinder
No. of Hidden Layers	6	8
No. of Neurons per Hidden Layer	100	200
No. of Trainable Parameters	51,102	286,804
Learning Rate	0.002	0.1
Optimization Algorithm	Adam [52]	Adam [52]
No. of Epochs	1000	10000
Loss Function	Mean Squared Error	Mean Squared Error
Hidden Layers Activation	ReLU	ReLU
Output Layer Activation	Linear	Linear
Size of Training Set	1100	3500
Size of Testing Set	100	200

Table 3: Hyper-Parameters of MLPNN

Hyper-parameters of the MLPNN for both the cases are listed in table 3. These hyper-parameters are tuned by using 10% of the training data for validation. The trained network is tested on a separate unseen dataset. For a dataset with sample size m , let $\mathbf{y}^s = [y_1^s, y_2^s, \dots, y_m^s]$ and $\mathbf{y}^n = [y_1^n, y_2^n, \dots, y_m^n]$ denote predictions of the variable y using numerical simulations and neural networks respectively. The coefficient of determination (R^2) [53] is used to estimate accuracy of the neural networks.

$$\text{Accuracy: } R^2 = 1 - \frac{\sum_{i=1}^m (y_i^s - y_i^n)^2}{\sum_{i=1}^m (y_i^s - \text{mean}(\mathbf{y}^s))^2} \quad (2)$$

Percentage errors are defined as follows:

$$\text{Average percent error: } 100 \times \frac{1}{m} \frac{\sum_{i=1}^m ||y_i^s - y_i^n||}{\max_{i=1}^m ||y_i^s||} \quad (3)$$

$$\text{Maximum percent error: } 100 \times \frac{\max_{i=1}^m ||y_i^s - y_i^n||}{\max_{i=1}^m ||y_i^s||} \quad (4)$$

		Single		Double Elliptic Cylinder			
		Elliptic Cylinder		Upstream		Downstream	
		Lift	Drag	Lift	Drag	Lift	Drag
Accuracy	Training	0.999936	0.999954	0.998668	0.998507	0.997685	0.998775
	Testing	0.999791	0.999821	0.997543	0.998020	0.988764	0.997606
Average	Training	0.3050	0.0717	1.317	0.4091	0.6759	0.4286
Percent Error	Testing	0.5495	0.1333	1.699	0.4508	1.239	0.6132
Maximum	Training	1.327	0.3679	6.807	6.235	6.706	2.609
Percent Error	Testing	2.063	0.9228	11.18	2.406	17.90	4.748

Table 4: Accuracy and Error of MLPNN

The error and accuracy for training and testing sets are listed in table 4. For a perfect model which fits the data exactly, R^2 takes a value of unity [53]. In the case of practical models, R^2 is always less than unity. R^2 value close to unity indicates high accuracy. Thus, low errors and high accuracy show that the networks are successful in estimating the lift and drag coefficients for both the cases. Moreover, similar error estimates for training and testing sets indicate that the chosen hyper-parameters are optimal and the networks have low variance. The estimates of drag and lift coefficients obtained from numerical simulations and neural networks for testing datasets are plotted in figs. 5 and 6. Both the axes are scaled to range $[0, 1]$ using the minimum and maximum values of the numerical estimates. It can be seen that most of the points lie on the ideal trend line $y = x$ indicating high accuracy of the networks. It should be noted that there are always a few outliers which show

slightly higher errors.

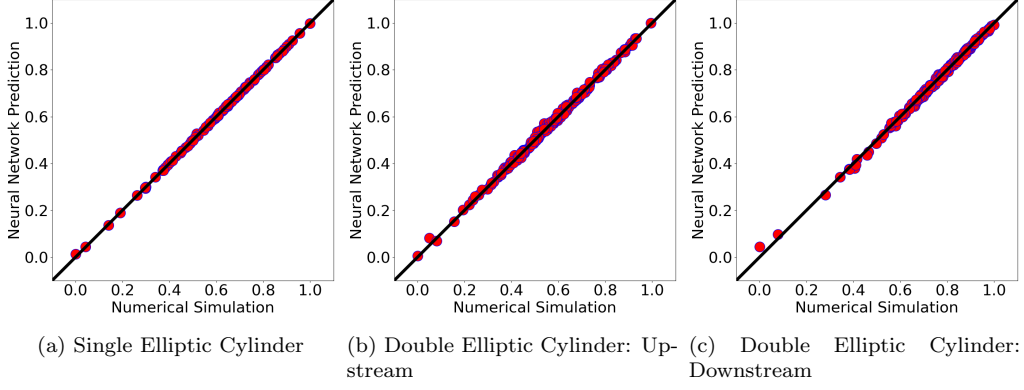


Figure 5: Drag Coefficient (Scaled): Comparison of Numerical Simulation and Neural Network Prediction

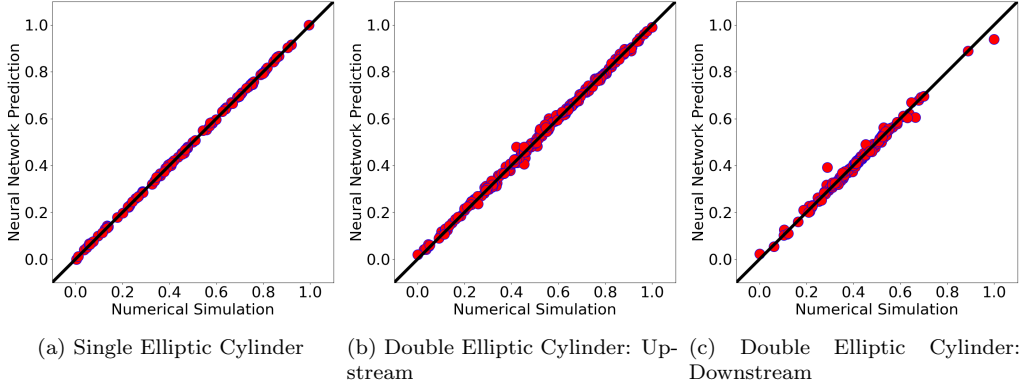


Figure 6: Lift Coefficient (Scaled): Comparison of Numerical Simulation and Neural Network Prediction

3.2. Convolutional Neural Network (CNN) for Prediction of Velocity and Pressure Fields

CNN [54] specializes in data that has grid-like topology. Image based or time series datasets have such grid-like structure. For image based datasets, MLPNN is inefficient since flattening an image gives a vector with huge size

thus, having too many weights and biases to be trained. CNN on the other hand uses the correlation between neighboring pixel values efficiently. In this case, the velocities and pressure at the neighboring points in the domain are correlated because of the underlying physics (the Navier–Stokes equations). Pooling, upsampling, convolution and transpose convolution are some of the common layers used in building a CNN [1].

In this work, we only use the dense and transpose convolution layers. Dense layers are briefly described in section 3.1. For further details of dense layers, please refer to our previous work [7]. Velocity and pressure contours are represented as images. In order to train a CNN with Reynolds number and geometric parameters as inputs, it is necessary to decompress the lower dimensional information to obtain images as outputs. There are various up-sampling techniques to decompress images such as interpolation and nearest neighbor algorithm [55] which have predefined structure and thus, do not learn with training data. Transpose convolution layer on the other hand, uses a kernel which is trained using the back propagation algorithm [1]. If an input image with size (R_I, C_I) is fed to a transpose convolution layer, size of the output image (R_O, C_O) is given by the following equations [56, 57]:

$$\begin{aligned} R_O &= (R_I - 1)S[1] + K[1] - 2P_I[1] + P_O \\ C_O &= (C_I - 1)S[2] + K[2] - 2P_I[2] + P_O \end{aligned} \tag{5}$$

where, S , K , P_I and P_O denote stride, kernel size and number of pixels used for padding of input and output respectively. Note that the stride, kernel size and input padding can be different for rows and columns. Hence, these are pairs for two dimensional images. Figure 7 shows a small example where,

an input image of size $(2, 2)$ is decompressed into an image of size $(4, 4)$ using a stride and kernel of size $(2, 2)$ without any padding. Color coding is used to show the flow of information. For instance, the top left 2×2 part of the output is obtained by multiplying X_{11} with the kernel. For example, an input image of size $(100, 100)$ with stride of $(2, 2)$ and kernel size of $(3, 3)$ will give an output of size $(201, 201)$ if no padding is used (eq. (5)). Keras API of TensorFlow can fine tune the output size to double the input size i.e., $(200, 200)$ by using appropriate input and output padding. Thus, in a nutshell, transpose convolution with a stride of 2 can be used to double the image size. Note that a stride of $(2, 1)$ or $(1, 2)$ doubles only one dimension of the image.

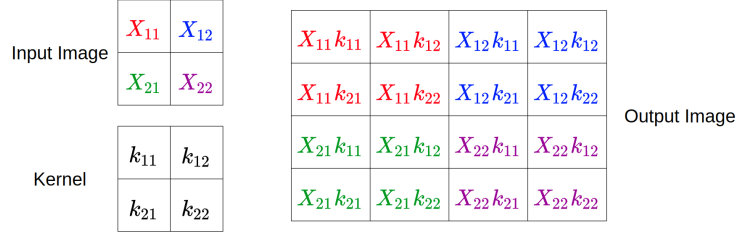


Figure 7: Example of Transpose Convolution with Stride: $(2, 2)$, Kernel size: $(2, 2)$

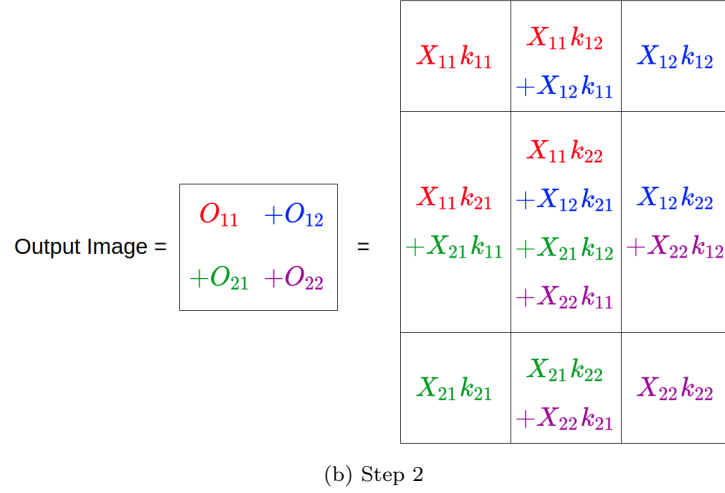
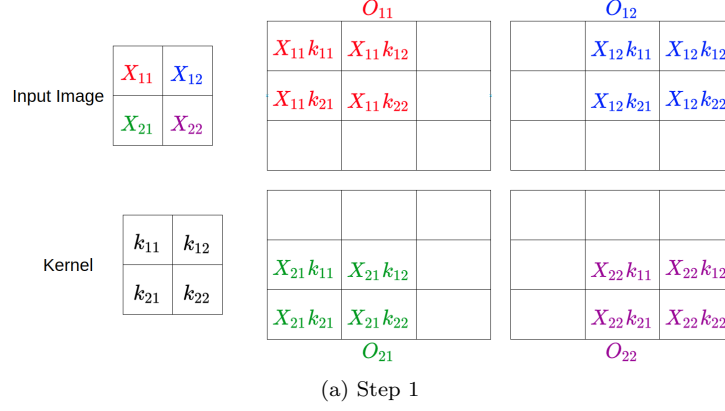


Figure 8: Example of Transpose Convolution with Stride: (1, 1), Kernel size: (2, 2)

Transpose convolution layer can also be used when the output is of the same size as input by setting stride to (1, 1). Figure 8 shows one such example of unit stride. Kernel of size (2, 2) is operated on an input image of size (2, 2) to give an output image of size (3, 3) with no padding (eq. (5)). For the sake of understanding, the operation is broken down into two steps. In the first step, each entry of the input image is operated on the kernel to give 4 matrices: O_{11} , O_{12} , O_{21} and O_{22} . These are similar to the previous example. But since

the stride is set to $(1, 1)$ in this case, these 4 matrices have an overlap. Second step shows the final output obtained after adding the individual matrices. It can be seen that the 4 corners have single term since there is no overlap. The central row and column have 2 entries added together. The central cell has components of all the 4 matrices and thus, has 4 terms added. As mentioned before, TensorFlow can fine tune the padding such that the input and output are of same sizes. Some more examples of transpose convolution layers with padding are discussed by Dumoulin and Visin [56]. In practice, multiple two dimensional matrices are stacked together to form a three dimensional tensor. The depth of the cube is called as channel. The transpose convolution operator is applied on each input channel and added together with a bias term followed by non-linear activation function to obtain a channel of the next layer. Each channel has a different kernel matrix and bias which are obtained by minimizing the loss function on the training data.

In the current work, CNN is trained on the simulation domain cropped to 8 units upstream, 12 units downstream and 10 units on top and bottom of the center for the case of single elliptic cylinder. This small window is chosen for training the network since we are not interested in the contours away from the elliptic cylinder. A lattice point layout is used to generate a structured grid with 10000 ($= 100 \times 100$) points. The data obtained on unstructured grid from COMSOL is interpolated to a structured grid using a piecewise cubic method. This gives images of velocity and pressure contours with a resolution of 100×100 pixels.

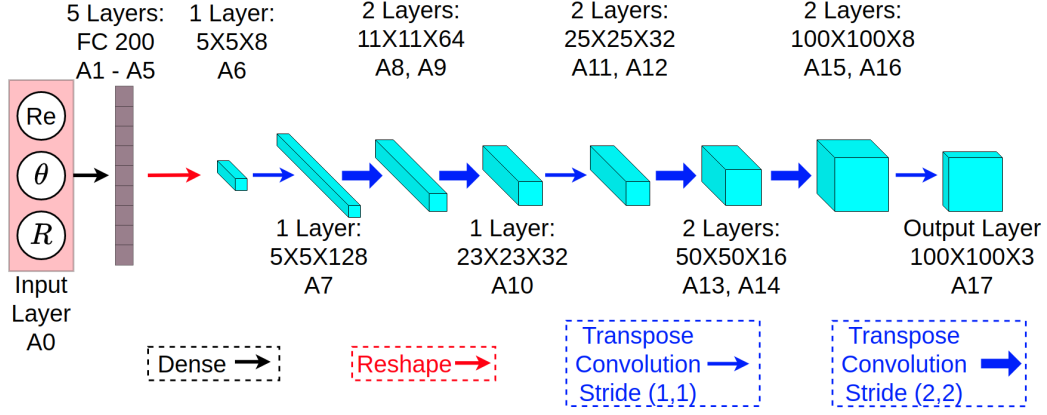


Figure 9: Case of Single Elliptic Cylinder: CNN for Estimation of Pressure and Velocities

Figure 9 shows a schematic of the CNN used for the case of single elliptic cylinder. Multiple dense fully connected (FC) and transpose convolution layers are stacked together to form a deep network. For the sake of clarity, the layers are numbered and connections are color coded. Identical layers which are repeated twice are shown only once in the diagram. The input layer (A0) is a dense layer with 3 neurons: Reynolds number, angle of attack and the ratio of major to minor axis. It is connected to 5 fully connected layers with 200 neurons each (A1 – A5). A5 is reshaped into a three dimensional tensor of size $5 \times 5 \times 8$. Thus, layer A6 consists of 5×5 images with 8 channels. Transpose convolution with kernel size of (3, 3) is used for all the subsequent layers. A6 is connected to A7 with a stride of (1, 1) so that the image size is the same. More channels improve the network accuracy since it increases the number of kernels and biases. This also adds to the computational expense during training. Hence, it is customary to have larger number of channels on smaller images and to reduce the number of channels as the image size grows. Thus, A7 has 128 channels the number goes down subsequently. From A7 to

A8 the image size roughly doubles to 11×11 and number of channels halves to 64. For this connection, a stride of (2, 2) is used without any padding. Layer A9 is identical to A8 connected by a transpose convolution operator of stride (1, 1) with padding. A9 to A10 connection is similar to the A7 to A8 connection. A11 is obtained from A10 by using a stride of (1, 1) without padding and thus, the image size slightly increases. A12 is identical to get A11. Similar operations are continued by setting appropriate padding and strides to double the image size and halve the number of channels. Finally, A16 is obtained, which has the desired image size of the output contours (100×100) and 8 channels. The output layer (A17) has only 3 channels: velocity components (x and y) and pressure.

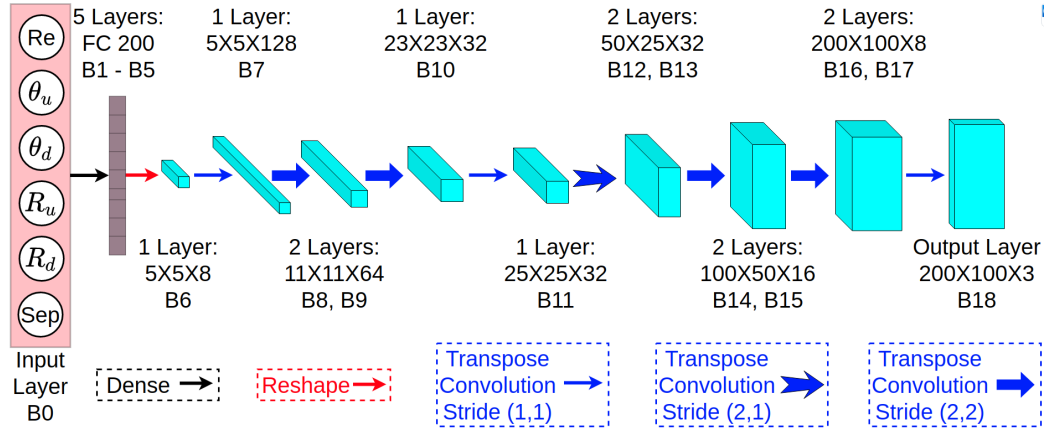


Figure 10: Case of Double Elliptic Cylinder: CNN for Estimation of Pressure and Velocities

The strategy used for the case of double elliptic cylinder is discussed here. The simulation domain is cropped to 10 units upstream, 30 units downstream and 10 units on top and bottom of the center of the upstream elliptic cylinder. A lattice point layout is used to generate a structured grid with 20000 ($= 200 \times 100$) points. The data obtained on unstructured grid

from COMSOL is interpolated to a structured grid using a piecewise cubic method. This gives images of velocity and pressure contours with a resolution of 200×100 pixels. Since the domain size is double in the flow direction, 200 pixels are used. Architecture of the CNN for the case of double elliptic cylinder (shown in fig. 10) is similar to the previously described CNN. Hence, only the differences are highlighted here. The input layer (B0) has 6 neurons: Reynolds number, angles of attack and ratios of both the elliptic cylinders and the separation distance between them. In this case, the output image is rectangular having 200 and 100 pixels in the flow and normal directions respectively. Thus, there is an additional connection of stride (2, 1) between B11 and B12 transforming square to rectangular images.

	Case of Single Elliptic Cylinder	Case of Double Elliptic Cylinder
Total No. of Hidden Layers	15	16
No. of Neurons per Dense Layer	200	200
No. of Trainable Parameters	330,075	339,987
Learning Rate	0.2	0.2
Optimization Algorithm	Adam [52]	Adam [52]
No. of Epochs	4000	2500
Loss Function	Mean Squared Error	Mean Squared Error
Hidden Layers Activation	ReLU	ReLU
Output Layer Activation	Linear	Linear
Size of Training Set	1800	3500
Size of Testing Set	100	200

Table 5: Hyper-Parameters of CNN

Table 5 lists down various hyper-parameters of both the CNNs. Trained networks are tested on a separate unseen dataset. The definitions of errors and accuracy is identical to the MLPNN case (eqs. (2) to (4)). Accuracy of

more than 0.985 and average error less than 0.4% for all the cases shows that the CNNs are successful. Also, similar error and accuracy for the training and testing data indicates that there is no over-fitting. Although the maximum error is high, we found that it is localized at few pixels near the cylindrical surface. The main cause may be the sudden jump condition of velocities and pressure at the surface since inside the elliptic cylinder, there is no physical data available.

		Single Elliptic Cylinder			Double Elliptic Cylinder		
		x Vel	y Vel	Pressure	x Vel	y Vel	Pressure
Accuracy	Training	0.999134	0.994501	0.997055	0.998540	0.986541	0.990373
	Testing	0.997055	0.994110	0.996902	0.998699	0.986304	0.990262
Average Percent Error	Training	0.2730	0.1287	0.1160	0.2583	0.1879	0.1809
	Testing	0.2898	0.1353	0.1212	0.3351	0.2412	0.2357
Maximum Percent Error	Training	23.65	33.76	23.12	39.37	35.85	34.70
	Testing	26.25	24.54	26.73	37.43	45.15	36.32

Table 6: Accuracy and Error of CNN

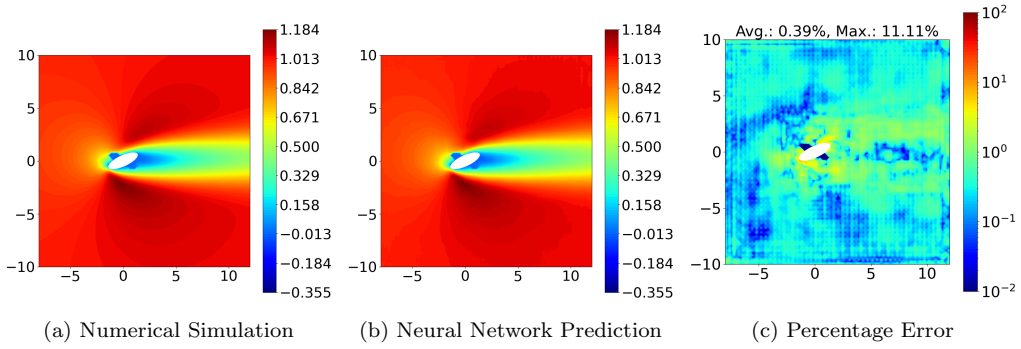


Figure 11: x-Velocity Single Elliptic Cylinder: Comparison of Numerical Simulation and Neural Network (Reynolds No.: 18, Angle: 25° , Aspect Ratio: 2.99)

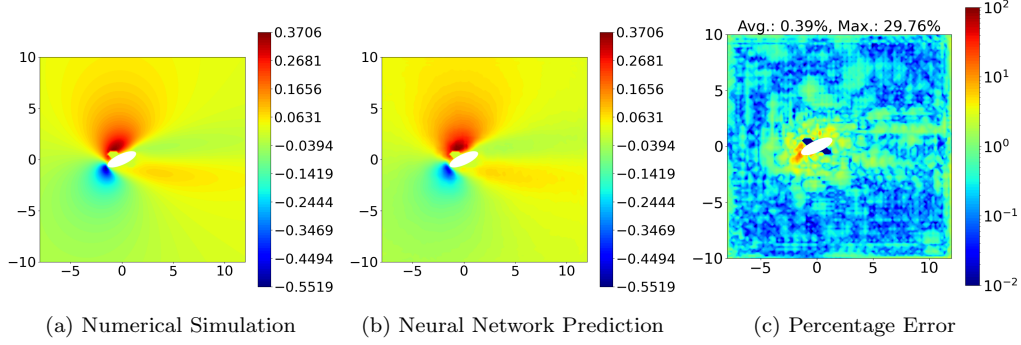


Figure 12: y -Velocity Single Elliptic Cylinder: Comparison of Numerical Simulation and Neural Network (Reynolds No.: 18, Angle: 25° , Aspect Ratio: 2.99)

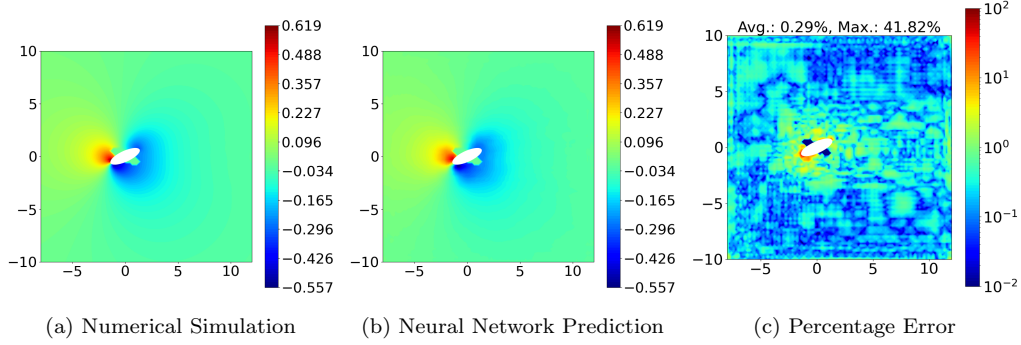


Figure 13: Pressure Single Elliptic Cylinder: Comparison of Numerical Simulation and Neural Network (Reynolds No.: 18, Angle: 25° , Aspect Ratio: 2.99)

Figures 11 to 13 plot comparison of contours obtained by CNN and COM-SOL together with the difference between them. The CNN is able to estimate remarkably similar contours. The percentage error is plotted with a color-bar having logarithmic scale ranging from 0.01% to 100%. The average and maximum percentage errors are mentioned in the plot titles. As discussed before, the maximum error is localized over a small region near the cylinder. The average error is less than 1%. A neural network is expected to have a few outliers. But it can be seen that the network is able to capture all the

important features such as stagnation region and reattachment. Figures 14 to 16 are similar contour plots for the case of double elliptic cylinder. This CNN is also successful in learning the flow features despite of some outliers with localized regions of high errors.

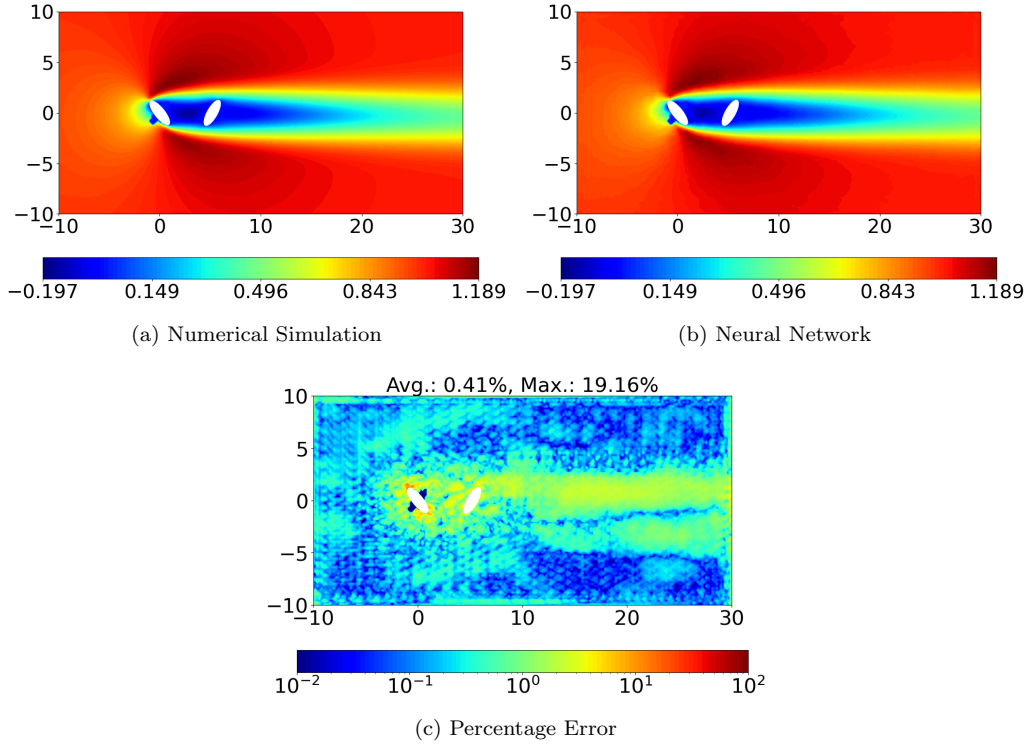


Figure 14: x-Velocity Double Elliptic Cylinder: Comparison of Numerical Simulation and Neural Network (Reynolds: 32, Angle upstream: 129° , Aspect ratio upstream: 2.92, Angle downstream: 61° , Aspect ratio downstream: 2.83, Cylinder separation: 5.20)

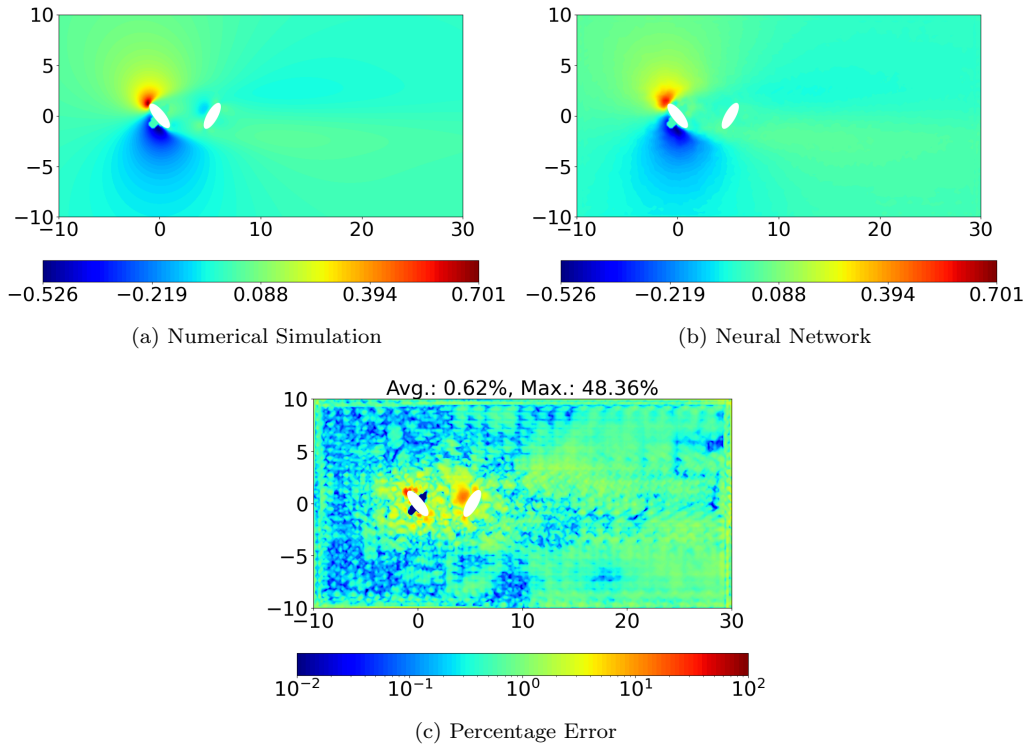


Figure 15: y-Velocity Double Elliptic Cylinder: Comparison of Numerical Simulation and Neural Network (Reynolds: 32, Angle upstream: 129° , Aspect ratio upstream: 2.92, Angle downstream: 61° , Aspect ratio downstream: 2.83, Cylinder separation: 5.20)

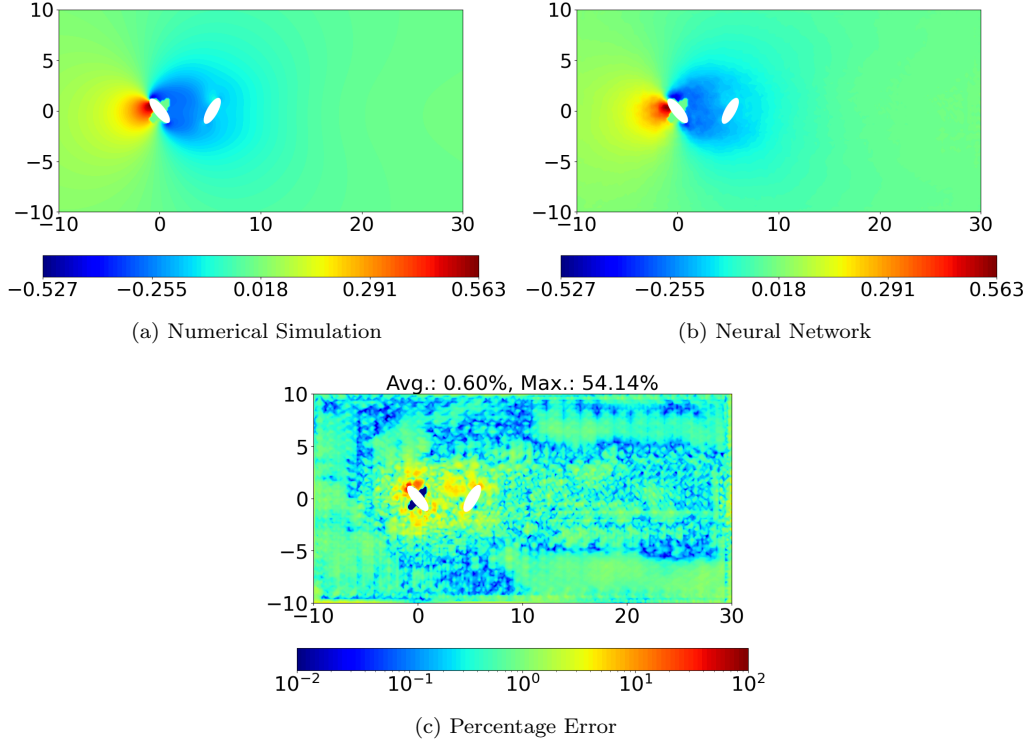


Figure 16: Pressure Double Elliptic Cylinder: Comparison of Numerical Simulation and Neural Network (Reynolds: 32, Angle upstream: 129° , Aspect ratio upstream: 2.92, Angle downstream: 61° , Aspect ratio downstream: 2.83, Cylinder separation: 5.20)

4. Application of the Neural Networks

4.1. Contours of Velocities and Pressure

The CNN described in section 3 can now be used to study the characteristics of the flow variables for any arbitrary combination (within the trained ranges) of Reynolds number, angles of attack, aspect ratios, and inter-cylinder spacing in case of cylinders in tandem. The CNN results can be generated almost instantaneously with good accuracy, as shown in section 3. In this section, we present results for a few selected cases for illustration. Figure 17 shows the contours of x-velocity, y-velocity, and pressure for

an arbitrarily selected parameter combination of Reynolds no. of 40, aspect ratio of 2 and angle of 135° . The cylinders are shown in white color, while positive and negative values of the variable are shown in color scale shown adjacent to the figures. The trends observed in the CNN pictures are as expected with the formation of a recirculation region with negative velocities, and negative pressure behind the cylinder, recovery of the wake and a stagnation region in front of the cylinder. The y-direction velocities also show the positive and negative deflection of the flow with asymmetry due to the angle of attack. The quantitative values of lift and drag will be presented in the next section.

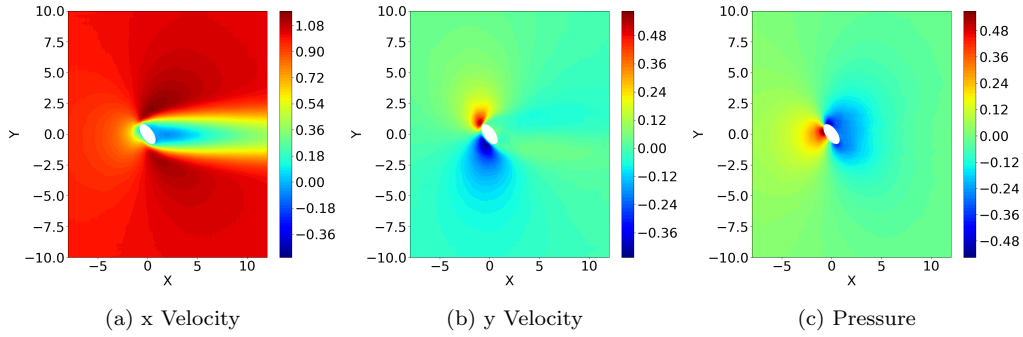


Figure 17: Reynolds No.: 40, Aspect Ratio: 2, Angle of Attack: 135°

The influence of the angle of attack for the same Re and aspect ratio is shown in fig. 18 for angle of 90° . Here, the elliptic cylinder is placed symmetrically about the horizontal centerline, thus giving symmetric contours. Notice that the results are shown only for the region (square of 20×20 units) on which the CNN is trained. As expected, the wake region is larger for 90° angle of attack than that for 0° (not shown). Also, when the angle is 90° , the major axis is facing the flow, giving a larger face area normal to the flow.

With angle 0° , we observe that there is no recirculation region behind the cylinder for this Reynolds number. This has been observed also by other investigators [44].

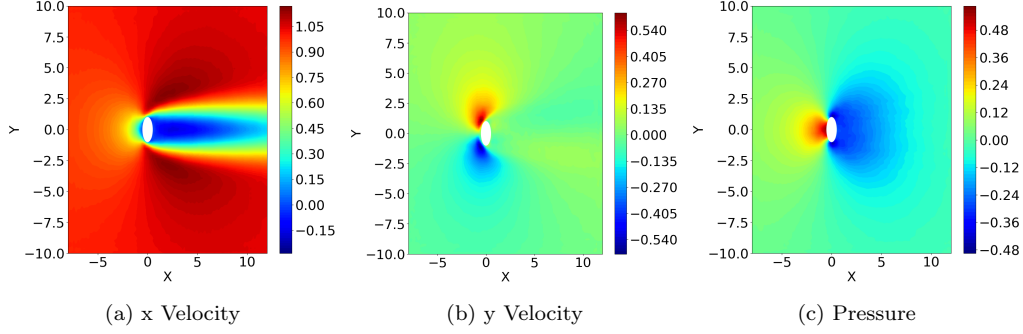


Figure 18: Reynolds No.: 40, Aspect Ratio: 2, Angle of Attack: 90°

A sample result of velocities and pressure distributions at aspect ratio of 3, Reynolds no. of 40, and angle of attack of 135° is shown in fig. 19. Here, the wake length is expectedly larger than that for aspect ratio of 2 because of the larger body size (note that the minor axis is always fixed at unit length). When the cylinder is placed horizontally at 0° angle (fig. 20), there is no negative flow behind it because of the lower than critical Reynolds number. This observation is consistent with other previous studies.

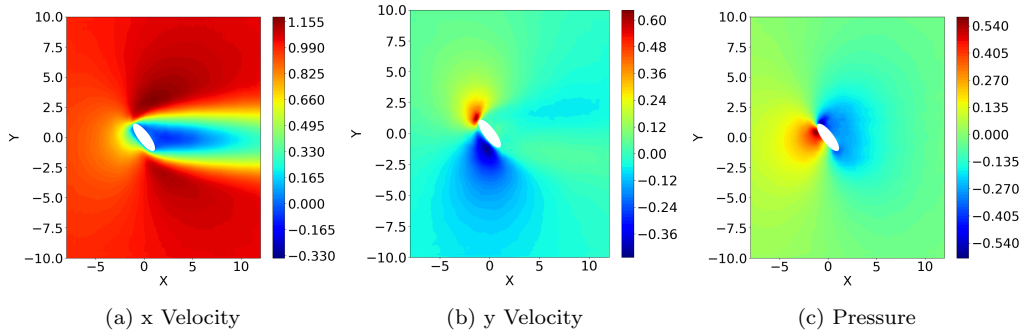


Figure 19: Reynolds No.: 40, Aspect Ratio: 3, Angle of Attack: 135°

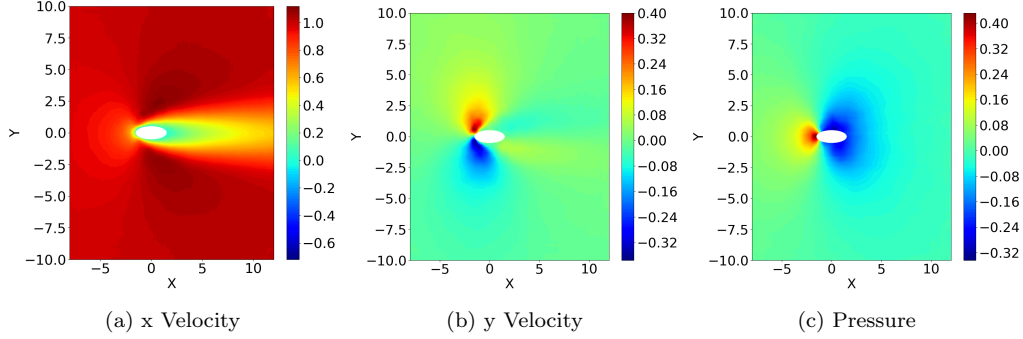


Figure 20: Reynolds No.: 40, Aspect Ratio: 3, Angle of Attack: 0°

The effect of adding a second cylinder in the wake of the first cylinder is shown in figs. 21 to 23. For a twin cylinder case, we can also vary the aspect ratio, angles of attack and the separation between the two cylinders independently. This gives a wide parameter space to explore. The CNN for the tandem cylinder case is separately trained with initial simulation parameters chosen on a 6-dimensional Latin Hypercube. The CNN so trained is applied to illustrate three different configurations here. Figure 21 shows velocities and pressure for the case of the upstream cylinder at 90° and the downstream cylinder at 45° with separation distance of 5 units length. As expected, the wake coming out of the first cylinder is symmetric for some distance, but then gets distorted upon the interaction with the wake of the second cylinder, which is placed at an angle. However, since the cylinder is placed in the wake of the first cylinder where the velocities are low, the effects on the second cylinder are relatively small on the downstream flow. Similar plots are shown in fig. 22 for a spacing of 9 units for which the interaction between the two wake cylinders is nearly one-way only.

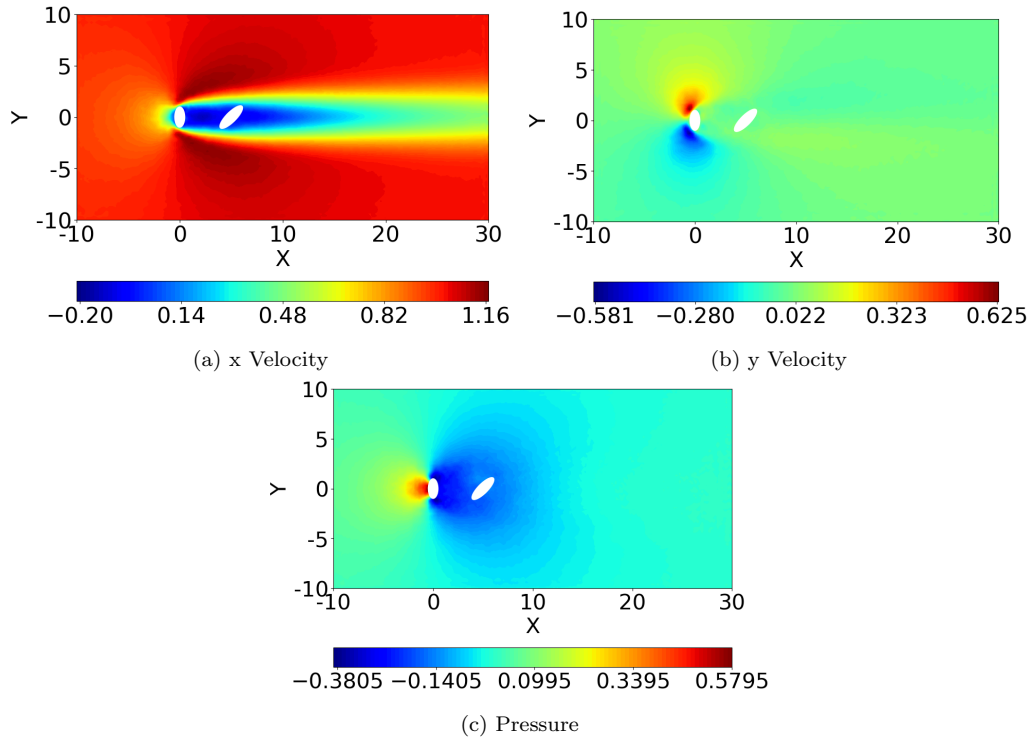


Figure 21: Reynolds No.: 40, Upstream Aspect Ratio: 2, Downstream Aspect Ratio: 3, Upstream Angle: 90° , Downstream Angle: 45° , Cylinder Separation: 5

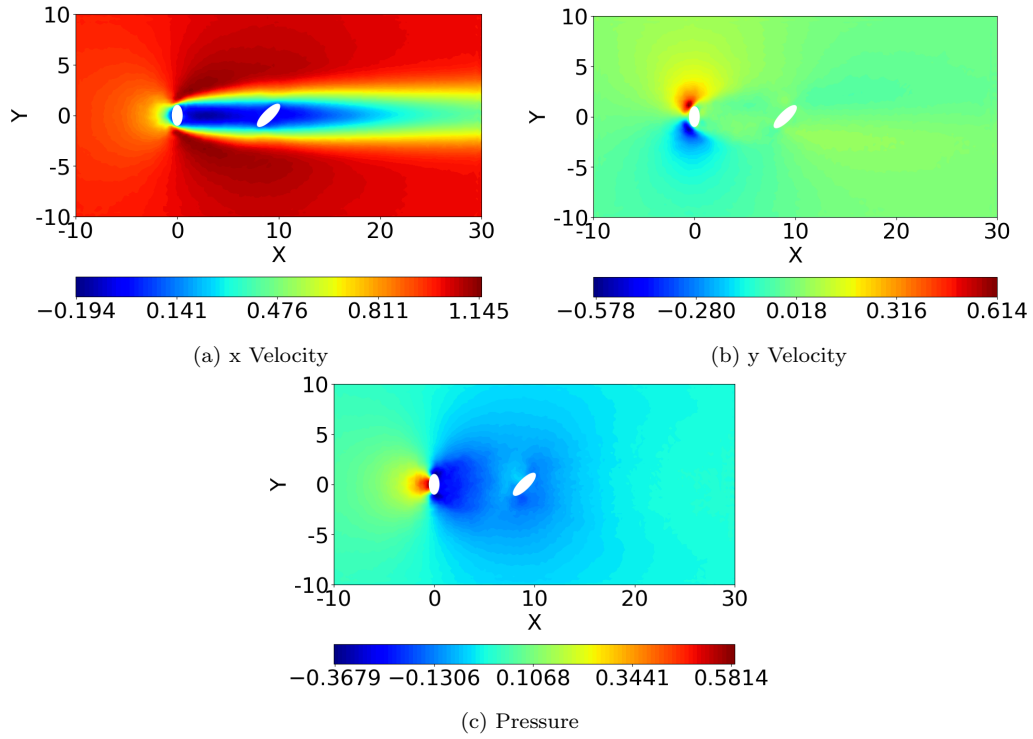


Figure 22: Reynolds No.: 40, Upstream Aspect Ratio: 2, Downstream Aspect Ratio: 3, Upstream Angle: 90° , Downstream Angle: 45° , Cylinder Separation: 9

Figure 23 shows a different combination of the parameters for the same Reynolds number. Again, the results are as expected, but the important aspect is that they could be generated in much smaller times than a full scale CFD calculation. Since the turnaround time is very small, these calculations are valuable as instructional tools in virtual laboratories.

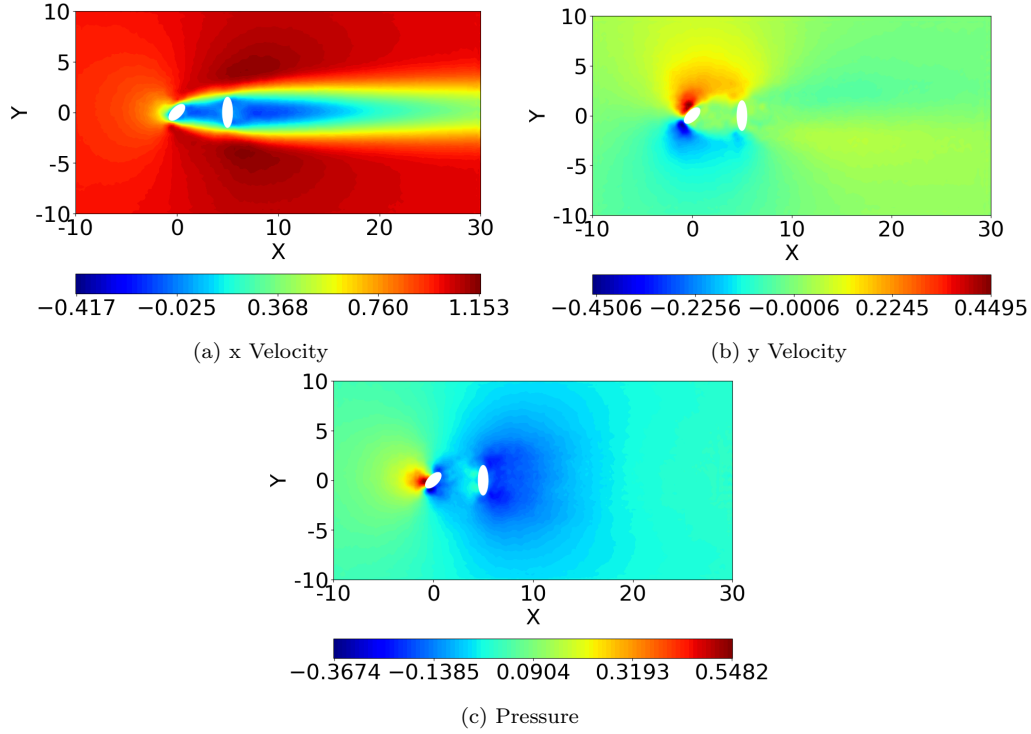


Figure 23: Reynolds No.: 40, Upstream Aspect Ratio: 2, Downstream Aspect Ratio: 3, Upstream Angle: 45° , Downstream Angle: 90° , Cylinder Separation: 5

4.2. Lift and Drag Coefficients

The MLPNN for lift and drag coefficients is now used to study their variation with aspect ratio, angle of attack and the flow Reynolds number (between 20 and 40). A pictorial variation as contour plots is first shown in figs. 24 and 25. Figure 24 shows the lift coefficients with angle of attack and aspect ratio as coordinate axes. The angle of 0° corresponds to a horizontal placement of the major axis, and the angle of attack is measured counter-clockwise. An angle of 90° corresponds to the major axis being vertical. As can be expected, the lift coefficients for 0° , 90° , and 180° angles of attack are zero, with maximum lift coefficients occurring around 45° and 135° . More-

over, for angle of attack of between $[0^\circ, 90^\circ]$, the major axis points in the first and third quadrant. Hence, the lift is negative since the force is acting in the downward direction.

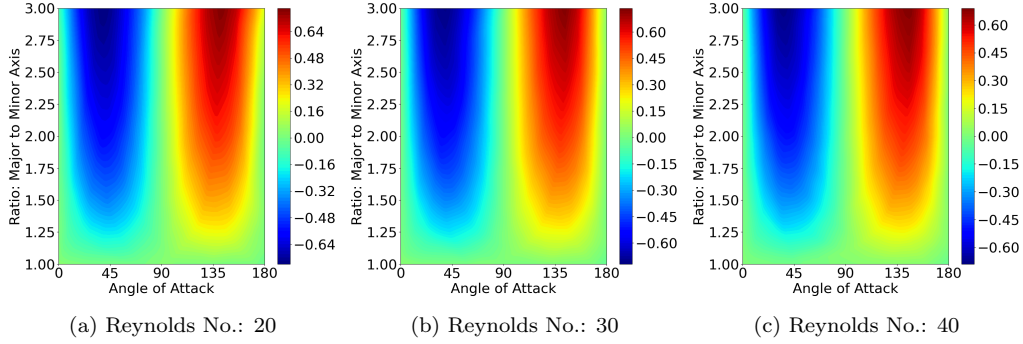


Figure 24: Case of Single Elliptic Cylinder: Lift Coefficient

Figure 25 shows the variation of the drag coefficient at the same three Reynolds numbers. The drag coefficient is always maximum at 90 degrees. The drag is the same for all angles of attack for the aspect ratio of unity (circular cylinder). For non-unity aspect ratios, the drag increases with angle of attack between 0° and 90° , and then decreases between 90° and 180° . The drag also increases with aspect ratio for any angle of attack. The drag, which includes both pressure drag and viscous shear stress, decreases with Reynolds number because of the lower viscosity. The present Reynolds number range is limited to a value for which all angles of attack give a steady flow.

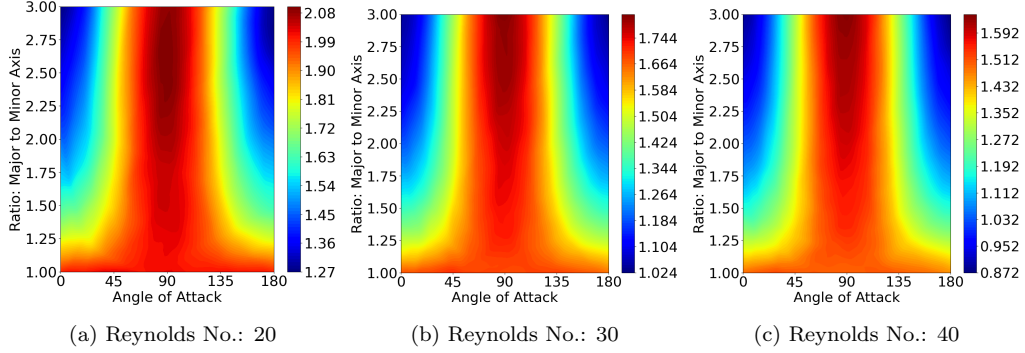


Figure 25: Case of Single Elliptic Cylinder: Drag Coefficient

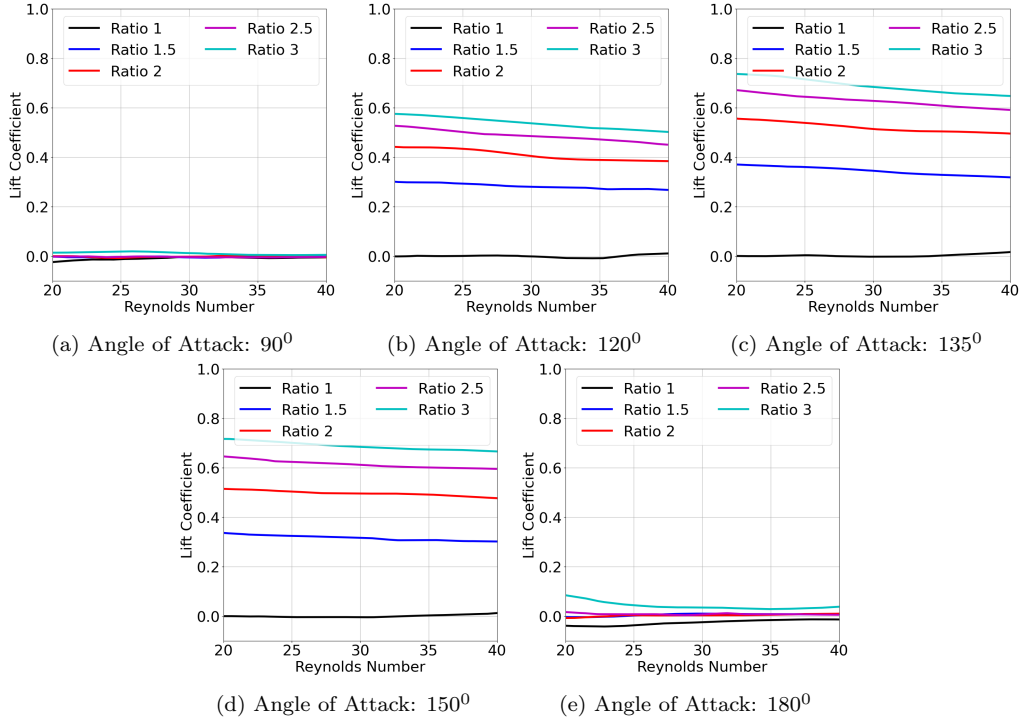


Figure 26: Case of Single Elliptic Cylinder: Lift Coefficient

We now discuss the same variations shown above by studying the trends through line plots. Figure 26 shows the lift coefficient for various angles of attack as a function of the Reynolds number. We first observe that the

neural network gives the lift coefficient for angles of attack of 0° , 90° and 180° to be nearly zero within a few percent error. For other angles between 90° and 180° , the lift coefficient is positive, and increases with aspect ratio. As the body becomes slimmer and slimmer, the separation length and the low pressure on the back side of the body increase, thus increasing the lift coefficient. Also, the surface area over which the pressure and normal stress forces act also increase. Thus, the lift coefficient becomes larger as the angle of attack passes 90 degrees. The effect of the aspect ratio is always seen to be monotonic for all angles of attack.

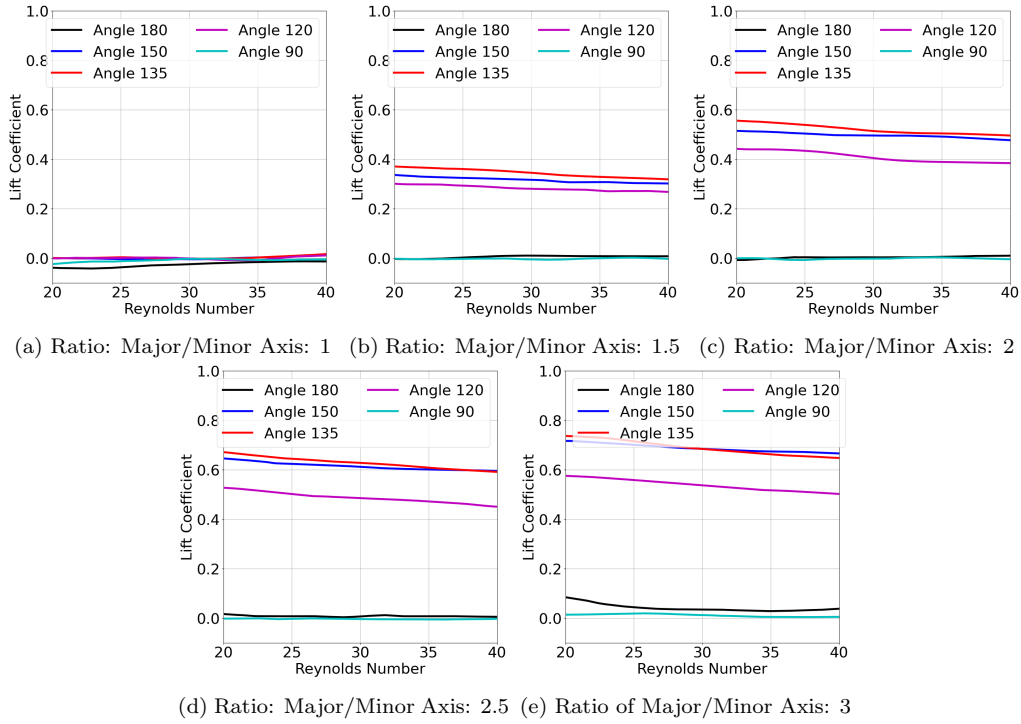


Figure 27: Case of Single Elliptic Cylinder: Lift Coefficient

It is also instructive to plot the variations of both lift and drag as a function of the Reynolds number. This effect is seen to be somewhat weak,

as negative pressure on the back side of the cylinder decreases only slightly with the Reynolds number. However, as seen earlier, the angle of attack has a predominant effect on the lift coefficient. Surprisingly, the lift coefficients for angle of attack of 150° and 135° are nearly the same for all aspect ratios. This is particularly the case for aspect ratios two and greater.

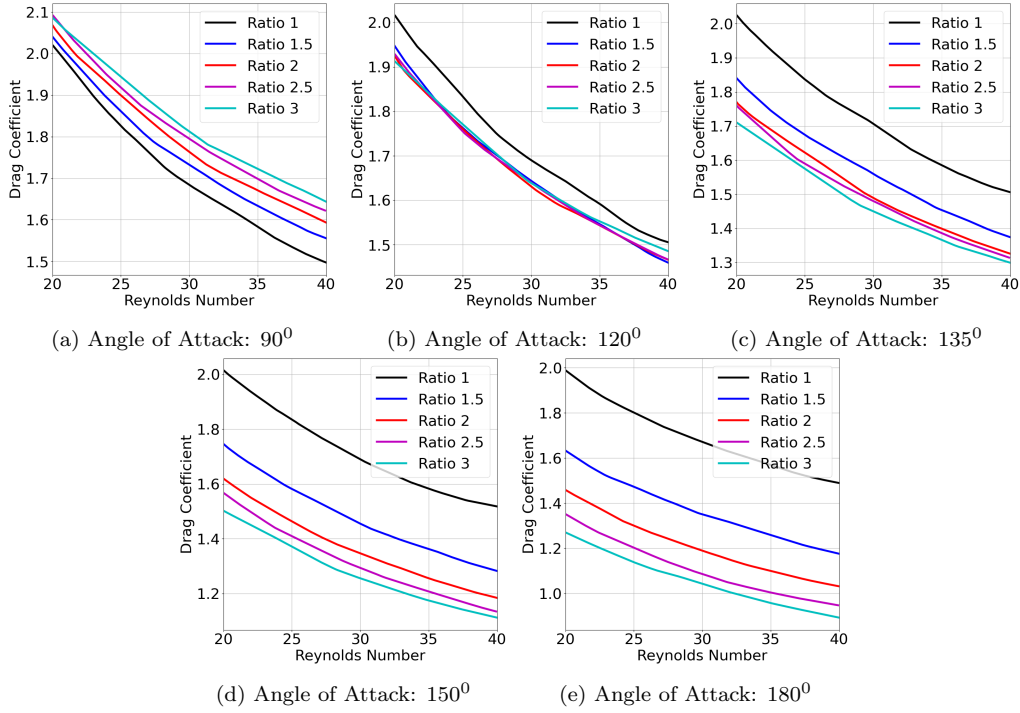


Figure 28: Case of Single Elliptic Cylinder: Drag Coefficient

The effect of Reynolds number on the drag coefficient, for various angles of attack, is shown in fig. 28 for different aspect ratios. First, for the case of unity aspect ratio, there is no effect of the angle of attack. The drag coefficient is the same at all angles of attack and reduces with Reynolds number. For non-unity aspect ratios, interesting trends are observed. For a vertical alignment (90°), the drag is higher than that of a cylinder for all

aspect ratios. However, as the cylinder is rotated counterclockwise to higher angles, the curves cross those of the circular cylinder and predict a lower drag coefficient. When the cylinder reaches a horizontal position (180°), the drag becomes smaller than the circular cylinder. As the aspect ratio is increased, the cylinder tends to get slimmer, so the drag due to wake formation and skin friction is reduced.

For tandem cylinders, there are six parameters, and hence the lift and drag coefficients vary over a six-dimensional space. We have arbitrarily selected two cases to demonstrate what can be obtained from the trained neural networks. We are currently developing a graphical interface which can be used to maneuver the complete space and easily compute the parametric variations. This interface can be used as a virtual laboratory experiment in fluid mechanics education.

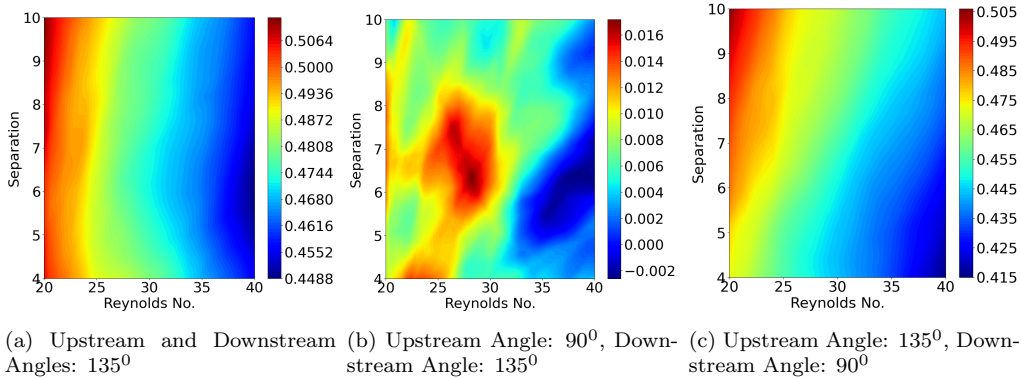


Figure 29: Case of Double Elliptic Cylinder: Lift Coefficient of Upstream Cylinder (Upstream and Downstream Aspect Ratio: 2)

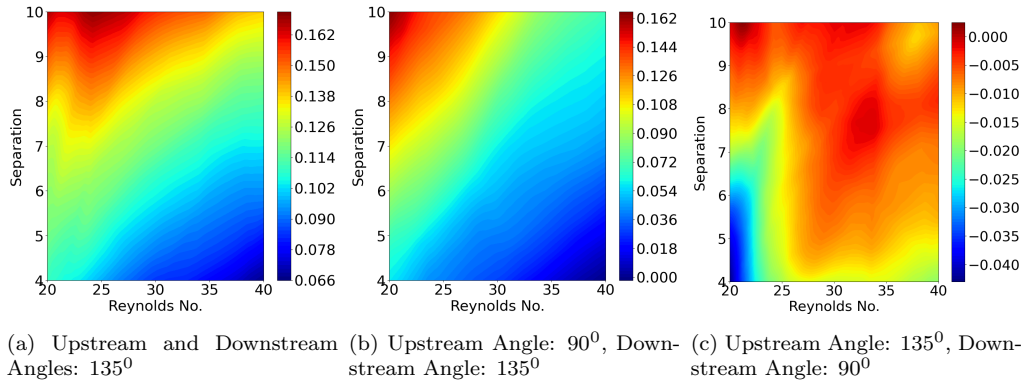


Figure 30: Case of Double Elliptic Cylinder: Lift Coefficient of Downstream Cylinder (Upstream and Downstream Aspect Ratio: 2)

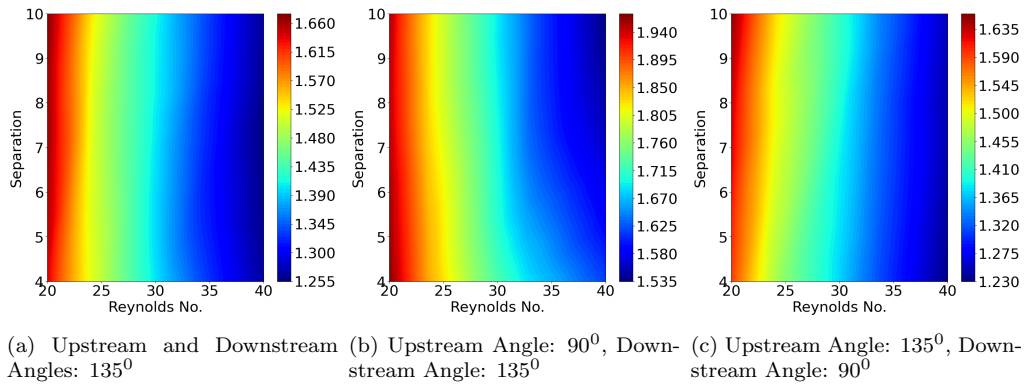


Figure 31: Case of Double Elliptic Cylinder: Drag Coefficient of Upstream Cylinder (Upstream and Downstream Aspect Ratio: 2)

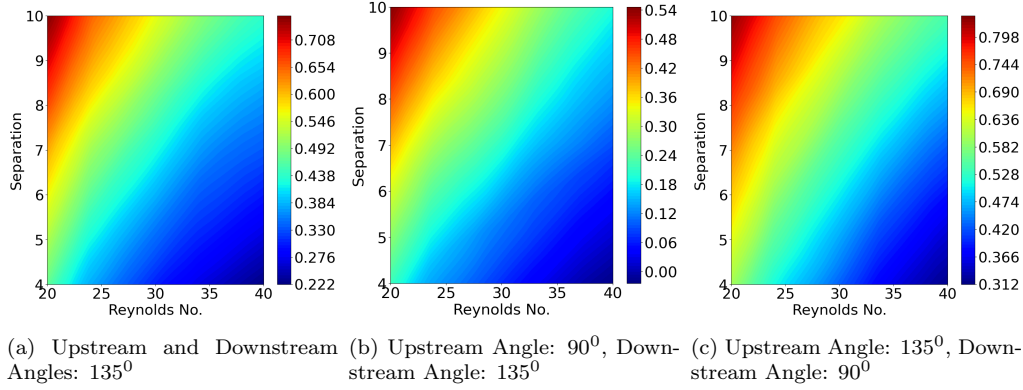


Figure 32: Case of Double Elliptic Cylinder: Drag Coefficient of Downstream Cylinder (Upstream and Downstream Aspect Ratio: 2)

4.3. Analysis of Sensitivity

Sensitivity can be defined as the effect of perturbation of an input on an output. Let Y be a scalar output dependent on a d -dimensional input vector $\mathbf{X} = [X_1, X_2, \dots, X_d]$. Let f denote the model which relates \mathbf{X} to Y i.e., $Y = f(\mathbf{X})$. In this case for instance, drag coefficient is a particular output (Y) as a function of inputs such as Reynolds number, ratio and angle of attack (3 dimensional vector \mathbf{X}) and the neural network is used as the model (f). Partial derivative of Y with respect to a particular input X_i can be used to estimate the sensitivity of Y to X_i . Since the partial derivative has to be evaluated at a particular value of $\mathbf{X} = \hat{\mathbf{X}}$, this gives an estimate of the local sensitivity at $\hat{\mathbf{X}}$. Response surfaces can be used to visualize local sensitivity. For example, slope of the contour lines in the fig. 25a is low for ratio of 1.25 and 0° angle of attack. Hence, in this region, the drag is more sensitive to the ratio than angle of attack. On the other hand, in the region of 2.5 ratio and 45° angle of attack, the contours are steep indicating that the drag is more sensitive to the angle. This example demonstrates

that the partial derivatives can vary significantly from one design point to another due to the nonlinearity of the model. Hence, for practical problems with nonlinear relationships, the local sensitivity analysis does not give any information of the entire design space.

In this work, we use the variance based analysis, also known as Sobol method [58] to estimate the global sensitivities of each output with respect to each input. The relation $Y = f(\mathbf{X})$ can be written as a summation of functions over individual inputs as follows:

$$Y = f(\mathbf{X}) = f_0 + \sum_{i=1}^d f_i(X_i) + \sum_{i<j}^d f_{i,j}(X_i, X_j) + \cdots + f_{1,2,\dots,d}(X_1, X_2, \dots, X_d) \quad (6)$$

where, f_0 is a constant, f_i is a function of single input X_i , $f_{i,j}$ is a function of two inputs X_i and X_j and so on. This summation has 2^d functions for a d dimensional input space. The decomposition is known as ANOVA (analysis of variances) if each of the functions has zero means:

$$\int f_{i_1, i_2, \dots, i_s}(X_{i_1}, X_{i_2}, \dots, X_{i_s}) dX_k = 0 \text{ for } k = i_1, i_2, \dots, i_s \quad (7)$$

It can be shown that if the above condition is satisfied, the functions are orthogonal and thus, the decomposition is unique [59]. If $f(\mathbf{X})$ is assumed to be square-integrable, squaring eq. (6) and integrating gives:

$$\int Y^2 d\mathbf{X} - f_0^2 = \sum_{s=1}^d \sum_{i_1 < \dots < i_s}^d \int f_{i_1, \dots, i_s}^2 dX_{i_1} \dots dX_{i_s} \quad (8)$$

Note that the terms such as $\int f_{i_1} f_{i_2} dX_{i_1} dX_{i_2}$ are zero due to orthogonality

and only the squared terms remain. The left hand side of eq. (8) is equal to variance of Y and the right hand side is a summation of variances due to groups of inputs. Hence, the total variance in Y is decomposed into variances attributed to individual inputs and interactions between them:

$$Var(Y) = \sum_{i=1}^d V_i + \sum_{i<j}^d V_{i,j} + \cdots + V_{1,2,\dots,d} \quad (9)$$

First order sensitivity index is defined as $S_i = V_i/Var(Y)$. Higher order indices such as $S_{i,j}$ are similarly defined. From eq. (9), it can be seen that these $(2^d - 1)$ indices are non-negative and sum to unity. Total Sobol index (S_{T_i}) for each input X_i is defined as sum of all the first and higher order indices with X_i in it. For example, for the case with 3 inputs, $S_{T_1} = S_1 + S_{1,2} + S_{1,3} + S_{1,2,3}$. Note that the sum of total indices is typically more than unity since the interaction terms are counted more than once. In this work, we analyze the total Sobol indices of each output (lift and drag coefficients) with respect to each input (Reynolds number, angle, ratio and separation). For simple functions, the integrals in eq. (8) can be evaluated analytically. For practical cases however, Monte-Carlo methods are used to estimate total Sobol indices. Brute force computation is $\mathcal{O}(N^2)$ where, N denotes the number of Monte-Carlo samples. Since N can be of the order of $10^5 \sim 10^6$, these computations are quite expensive even when surrogate models are used. Hence, we use the algorithm proposed by Saltelli et al. [59] which requires $\mathcal{O}(N(d+2))$ computations.

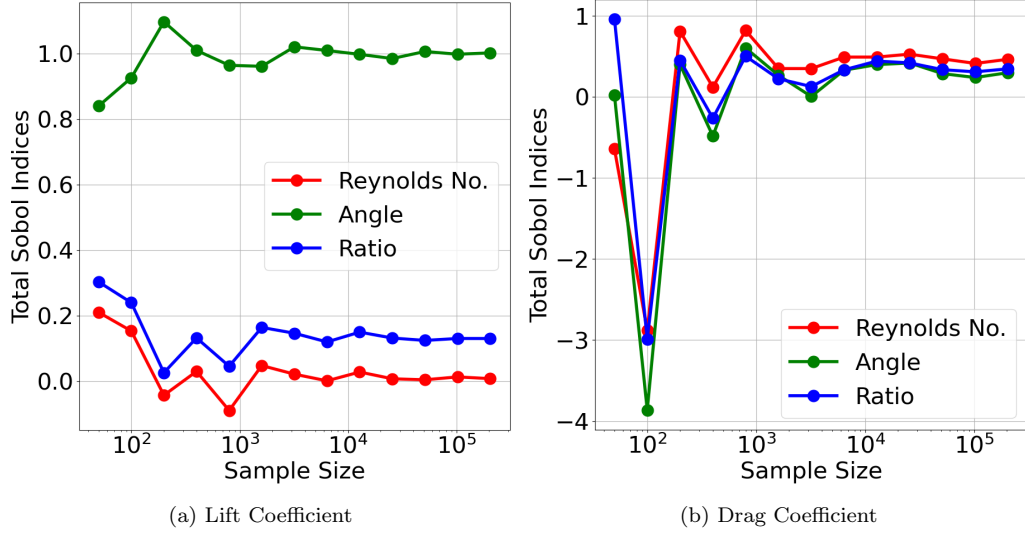


Figure 33: Case of Single Elliptic Cylinder: Estimation of Total Sobol Indices: Convergence of Monte-Carlo Method

The Monte-Carlo method obtains numerical estimates by repeated random sampling. The convergence error is $\mathcal{O}(1/\sqrt{N})$ [60] where, N is the sample size. In the absence of analytical solution, the sample size is increased until the estimates converge asymptotically. For the case of single cylinder, there are two outputs (lift and drag coefficients) and three inputs (Reynolds number, angle, ratio). Thus, convergence of $3 \times 2 = 6$ total Sobol indices is plotted in fig. 33. The sample size is increased from 50 to 2E5 by a factor of 2 each time. The lift and drag coefficients are estimated as a function of randomly generated sets of inputs using the MLPNN described before. The computational efficiency of neural network facilitates such high sample sizes. This demonstrates the benefit of coupling neural networks with numerical simulations. The initial estimates are inaccurate but stationarity is obtained as the sample size reaches close to 1E4. Thus, the average of last 5 estimates

is recorded as the converged value. Figure 34 is a bar chart with sensitivity of each output with respect to each input. As discussed before, the sum of total Sobol indices of both outputs is greater than unity. It can be seen that the lift coefficient is highly sensitive to the angle of attack and its dependence on the Reynolds number and aspect ratio is negligible. On the other hand, the drag is more sensitive to the Reynolds number but its sensitivity to the other inputs is also important.

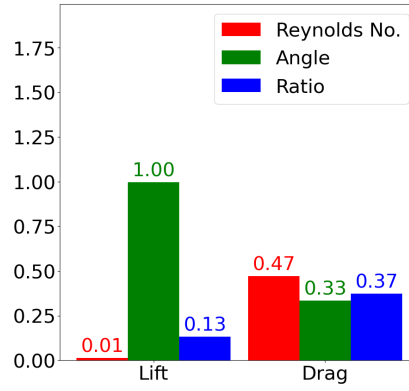


Figure 34: Case of Single Elliptic Cylinder: Total Sobol Indices: Sensitivity of Lift and Drag to 3 Inputs

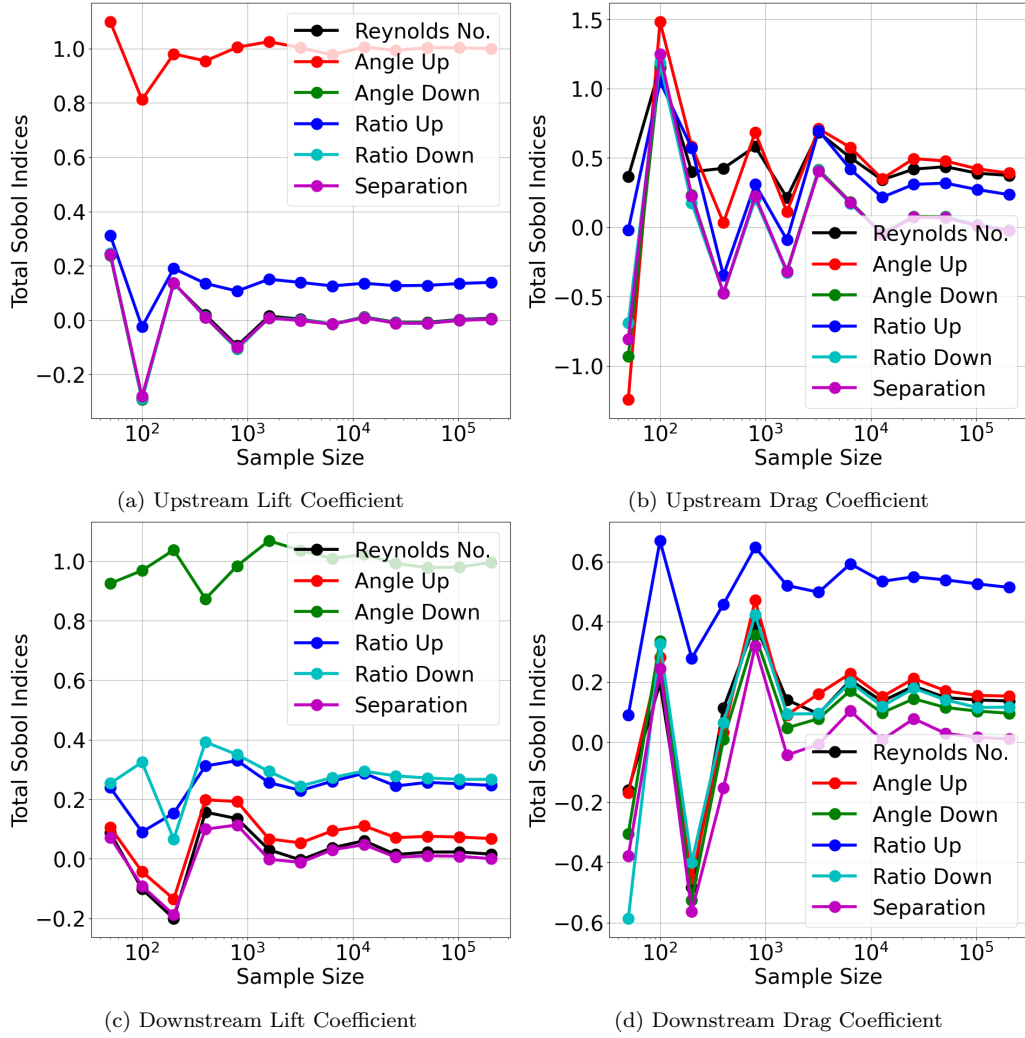


Figure 35: Case of Double Elliptic Cylinder: Estimation of Total Sobol Indices: Convergence of Monte-Carlo Method

For the case of double cylinders, there are 4 outputs and 6 inputs as shown in fig. 4b. Hence, there are $6 \times 4 = 24$ total Sobol indices. Figure 35 plots the convergence for sample size increased by a factor of 2 starting from 50. The stationarity is reached beyond 1E4 samples. Average of last five samples is recorded as the converged estimate in fig. 36. Similar to the case of single

cylinder, the lift coefficients of both the cylinders are highly sensitive to their respective angles of attack. The lift and drag of the upstream cylinder are not sensitive to the parameters of the downstream cylinder. This shows that the downstream cylinder has negligible effect on the upstream cylinder. Moreover, these sensitivity indices in fig. 36a are fairly close to the indices of single cylinder in fig. 34. On the other hand the downstream cylinder is affected significantly by the upstream cylinder. Thus, the downstream drag is most sensitive to the upstream ratio. Hence, the Sobol indices give insight in the system and highlight the underlying physics. The input parameters with higher indices should be tightly controlled since their stochastic variation affects the output significantly. Those inputs with lower indices can be loosely controlled as their impact on the output is minimal. This information can be used practically during the design and manufacturing stages.

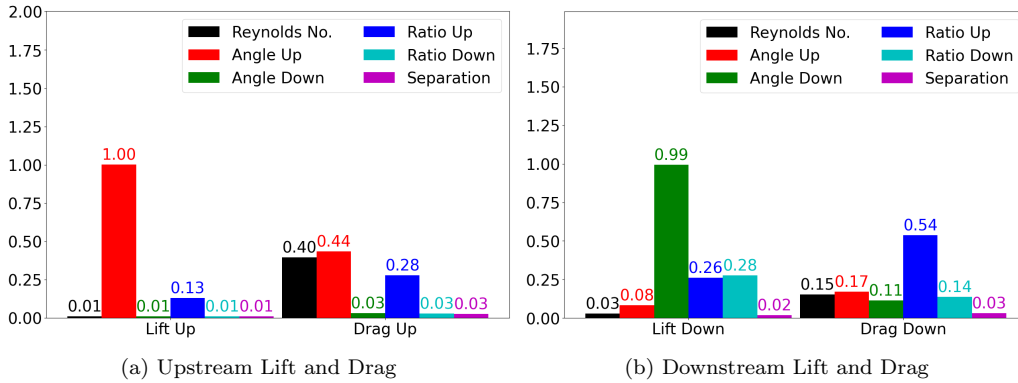


Figure 36: Case of Double Elliptic Cylinder: Total Sobol Indices: Sensitivity of Lift and Drag to 6 Inputs

5. Summary and Future Work

In the present paper, we have developed a convolutional neural network (CNN) for velocity and pressure fields of flow over single and tandem elliptic cylinders of arbitrary aspect ratios, angles of attack, inter-cylinder distance and flow Reynolds number. First, a large set of CFD simulations are conducted using the COMSOL Multiphysics computer program for parameters selected on a three (or six) dimensional Latin hypercube. The calculations stored images of horizontal and vertical velocity fields as well as coefficients of lift and drag. The data on flow and pressure fields are used to train the CNNs, while multilayer perceptron neural networks (MLPNNs) are trained for the lift and drag coefficients. Both types of networks are validated against separate ‘blind’ data sets, and good agreement is observed. The networks are demonstrated by computing the images for a couple of arbitrary sets of parameters. The parametric variation of the lift and drag coefficients for a single cylinder are presented for different Reynolds numbers, angle of attack, and aspect ratio of the cylinder.

A detailed sensitivity study is carried out using the MLPNN for lift and drag. The data sample for the sensitivity studies using the Monte-Carlo method is generated by the neural networks. The sample size is increased exponentially until the sensitivity coefficient converges to a value independent of the sample size. The study indicates which parameters are most influential over others in impacting the output variables. For a single cylinder, the lift coefficient is strongly dependent on the angle of attack, while the drag is a strong function of the Reynolds number. For the case of tandem cylinders, the lift on the upstream cylinder is most sensitive to its angle of attack,

while drag is equally sensitive to the Reynolds number and upstream angle of attack. The lift on the downstream cylinder is a strong function of the angle of attack of the upstream cylinder, while the drag on the downstream cylinder is most sensitive to the upstream cylinder aspect ratio.

The current study has been limited to the steady region. Efforts are underway to consider supercritical Reynolds number for which the flow will become unsteady with periodic shedding of vortices.

Data Availability Statement

The data that support the findings of this study are available from the corresponding author upon reasonable request.

References

- [1] I. Goodfellow, Y. Bengio, A. Courville, Deep Learning, MIT Press, 2016.
<http://www.deeplearningbook.org>.
- [2] G. C. Peng, M. Alber, A. B. Tepole, W. R. Cannon, S. De, S. Dura-Bernal, K. Garikipati, G. Karniadakis, W. W. Lytton, P. Perdikaris, et al., Multiscale modeling meets machine learning: What can we learn?, Archives of Computational Methods in Engineering (2020) 1–21.
- [3] J. Schmidhuber, Deep learning in neural networks: An overview, Neural networks 61 (2015) 85–117.
- [4] M. D. McKay, R. J. Beckman, W. J. Conover, A comparison of three methods for selecting values of input variables in the analysis of output from a computer code, Technometrics 42 (2000) 55–61.

- [5] R. L. Iman, J. C. Helton, J. E. Campbell, An approach to sensitivity analysis of computer models: Part i—introduction, input variable selection and preliminary variable assessment, *Journal of quality technology* 13 (1981) 174–183.
- [6] S. Shahane, N. Aluru, P. Ferreira, S. G. Kapoor, S. P. Vanka, Optimization of solidification in die casting using numerical simulations and machine learning, *Journal of Manufacturing Processes* 51 (2020) 130–141.
- [7] S. Shahane, N. R. Aluru, S. P. Vanka, Uncertainty quantification in three dimensional natural convection using polynomial chaos expansion and deep neural networks, *International Journal of Heat and Mass Transfer* 139 (2019) 613–631.
- [8] A. Takbiri-Borujeni, H. Kazemi, N. Nasrabadi, A data-driven surrogate to image-based flow simulations in porous media, *Computers & Fluids* 201 (2020) 104475.
- [9] J. Sun, J. Zhang, X. Zhang, W. Zhou, A deep learning-based method for heat source layout inverse design, *IEEE Access* 8 (2020) 140038–140053.
- [10] R. Han, Y. Wang, Y. Zhang, G. Chen, A novel spatial-temporal prediction method for unsteady wake flows based on hybrid deep neural network, *Physics of Fluids* 31 (2019) 127101.
- [11] T. Miyanawala, R. Jaiman, An efficient deep learning technique for the navier-stokes equations: Application to unsteady wake flow dynamics, *arXiv preprint arXiv:1710.09099* (2017).

- [12] J. Rabault, M. Kuchta, A. Jensen, U. Réglade, N. Cerardi, Artificial neural networks trained through deep reinforcement learning discover control strategies for active flow control, *Journal of Fluid Mechanics* 865 (2019) 281–302.
- [13] S. Bukka, R. Gupta, A. Magee, R. Jaiman, Assessment of unsteady flow predictions using hybrid deep learning based reduced order models, *arXiv preprint arXiv:2009.04396* (2020).
- [14] M. Ribeiro, A. Rehman, S. Ahmed, A. Dengel, Deepcfd: Efficient steady-state laminar flow approximation with deep convolutional neural networks, *arXiv preprint arXiv:2004.08826* (2020).
- [15] V. Sekar, Q. Jiang, C. Shu, B. Khoo, Fast flow field prediction over airfoils using deep learning approach, *Physics of Fluids* 31 (2019) 057103.
- [16] M. Raissi, G. Karniadakis, Hidden physics models: Machine learning of nonlinear partial differential equations, *Journal of Computational Physics* 357 (2018) 125–141.
- [17] F. Ogoke, K. Meidani, A. Hashemi, A. B. Farimani, Graph convolutional neural networks for body force prediction, *arXiv preprint arXiv:2012.02232* (2020).
- [18] M. Zhang, Z. Zheng, Y. Liu, X. Jiang, Numerical simulation and neural network study using an upstream cylinder for flow control of an airfoil, in: *Fluids Engineering Division Summer Meeting*, volume 59032, American Society of Mechanical Engineers, 2019, p. V002T02A045.

- [19] X. Jin, P. Cheng, W. Chen, H. Li, Prediction model of velocity field around circular cylinder over various reynolds numbers by fusion convolutional neural networks based on pressure on the cylinder, *Physics of Fluids* 30 (2018) 047105.
- [20] Z. Deng, C. He, Y. Liu, K. Kim, Super-resolution reconstruction of turbulent velocity fields using a generative adversarial network-based artificial intelligence framework, *Physics of Fluids* 31 (2019) 125111.
- [21] M. Braza, P. Chassaing, H. H. Minh, Numerical study and physical analysis of the pressure and velocity fields in the near wake of a circular cylinder, *Journal of fluid mechanics* 165 (1986) 79–130.
- [22] C. H. Williamson, Vortex dynamics in the cylinder wake, *Annual review of fluid mechanics* 28 (1996) 477–539.
- [23] S. Dennis, G.-Z. Chang, Numerical solutions for steady flow past a circular cylinder at reynolds numbers up to 100, *Journal of Fluid Mechanics* 42 (1970) 471–489.
- [24] D. J. Tritton, Experiments on the flow past a circular cylinder at low reynolds numbers, *Journal of Fluid Mechanics* 6 (1959) 547–567.
- [25] M. Zdravkovich, Flow around circular cylinders; vol. i fundamentals, *Journal of Fluid Mechanics* 350 (1997) 377–378.
- [26] A. Okajima, Strouhal numbers of rectangular cylinders, *Journal of Fluid mechanics* 123 (1982) 379–398.

- [27] A. Sharma, V. Eswaran, Heat and fluid flow across a square cylinder in the two-dimensional laminar flow regime, *Numerical Heat Transfer, Part A: Applications* 45 (2004) 247–269.
- [28] C. Jackson, A finite-element study of the onset of vortex shedding in flow past variously shaped bodies, *Journal of fluid Mechanics* 182 (1987) 23–45.
- [29] J. Robichaux, S. Balachandar, S. P. Vanka, Three-dimensional floquet instability of the wake of square cylinder, *Physics of Fluids* 11 (1999) 560–578.
- [30] A. Mukhopadhyay, G. Biswas, T. Sundararajan, Numerical investigation of confined wakes behind a square cylinder in a channel, *International journal for numerical methods in fluids* 14 (1992) 1473–1484.
- [31] F. M. Najjar, S. Vanka, Simulations of the unsteady separated flow past a normal flat plate, *International journal for numerical methods in fluids* 21 (1995) 525–547.
- [32] S. Dennis, J. Dunwoody, The steady flow of a viscous fluid past a flat plate, *Journal of Fluid Mechanics* 24 (1966) 577–595.
- [33] A. K. Saha, Far-wake characteristics of two-dimensional flow past a normal flat plate, *Physics of Fluids* 19 (2007) 128110.
- [34] M. Kemp, Leonardo da vinci’s laboratory: studies in flow, *Nature* 571 (2019) 322–324.

- [35] K. Shintani, A. Umemura, A. Takano, Low-reynolds-number flow past an elliptic cylinder, *Journal of Fluid Mechanics* 136 (1983) 277–289.
- [36] J. K. Park, S. O. Park, J. M. Hyun, Flow regimes of unsteady laminar flow past a slender elliptic cylinder at incidence, *International journal of heat and fluid flow* 10 (1989) 311–317.
- [37] S. K. Raman, K. Arul Prakash, S. Vengadesan, Effect of axis ratio on fluid flow around an elliptic cylinder—a numerical study, *Journal of fluids engineering* 135 (2013).
- [38] I. Paul, K. A. Prakash, S. Vengadesan, Numerical analysis of laminar fluid flow characteristics past an elliptic cylinder, *International Journal of Numerical Methods for Heat & Fluid Flow* (2014).
- [39] H. Lugt, H. Haussling, Laminar flow past an abruptly accelerated elliptic cylinder at 45 incidence, *Journal of Fluid Mechanics* 65 (1974) 711–734.
- [40] S. Taneda, The development of the lift of an impulsively started elliptic cylinder at incidence, *Journal of the Physical Society of Japan* 33 (1972) 1706–1711.
- [41] V. Patel, Flow around the impulsively started elliptic cylinder at various angles of attack, *Computers & Fluids* 9 (1981) 435–462.
- [42] T. Ota, H. Nishiyama, Y. Taoka, Flow around an elliptic cylinder in the critical reynolds number regime (1987).
- [43] M. Nair, T. Sengupta, Unsteady flow past elliptic cylinders, *Journal of fluids and structures* 11 (1997) 555–595.

- [44] Z. Faruquee, D. S. Ting, A. Fartaj, R. M. Barron, R. Carriveau, The effects of axis ratio on laminar fluid flow around an elliptical cylinder, *International Journal of Heat and Fluid Flow* 28 (2007) 1178–1189.
- [45] S. Dennis, P. Young, Steady flow past an elliptic cylinder inclined to the stream, *Journal of engineering mathematics* 47 (2003) 101–120.
- [46] H. Badr, S. Dennis, S. Kocabiyik, Numerical simulation of the unsteady flow over an elliptic cylinder at different orientations, *International journal for numerical methods in fluids* 37 (2001) 905–931.
- [47] S. D’alessio, S. Dennis, Steady laminar forced convection from an elliptic cylinder, *Journal of engineering mathematics* 29 (1995) 181–193.
- [48] S. D’alessio, S. Dennis, P. Nguyen, Unsteady viscous flow past an impulsively started oscillating and translating elliptic cylinder, *Journal of engineering mathematics* 35 (1999) 339–357.
- [49] T. Ota, H. Nishiyama, Flow around two elliptic cylinders in tandem arrangement (1986).
- [50] M. Abadi, A. Agarwal, P. Barham, E. Brevdo, Z. Chen, C. Citro, G. Corrado, A. Davis, J. Dean, M. Devin, S. Ghemawat, I. Goodfellow, A. Harp, G. Irving, M. Isard, Y. Jia, R. Jozefowicz, L. Kaiser, M. Kudlur, J. Levenberg, D. Mané, R. Monga, S. Moore, D. Murray, C. Olah, M. Schuster, J. Shlens, B. Steiner, I. Sutskever, K. Talwar, P. Tucker, V. Vanhoucke, V. Vasudevan, F. Viégas, O. Vinyals, P. Warden, M. Wattenberg, M. Wicke, Y. Yu, X. Zheng, *TensorFlow: Large-scale machine learning on heterogeneous systems*, 2015.

URL: <https://www.tensorflow.org/>, software available from tensorflow.org.

- [51] F. Chollet, et al., Keras, <https://keras.io>, 2015.
- [52] D. P. Kingma, J. Ba, Adam: A method for stochastic optimization, arXiv preprint arXiv:1412.6980 (2014).
- [53] A. C. Cameron, F. A. Windmeijer, An r-squared measure of goodness of fit for some common nonlinear regression models, *Journal of econometrics* 77 (1997) 329–342.
- [54] Y. LeCun, B. Boser, J. S. Denker, D. Henderson, R. E. Howard, W. Hubbard, L. D. Jackel, Backpropagation applied to handwritten zip code recognition, *Neural computation* 1 (1989) 541–551.
- [55] D. Mishra, Transposed convolution demystified, 2020. URL: <https://towardsdatascience.com/transposed-convolution-demystified-84ca81b4baba>.
- [56] V. Dumoulin, F. Visin, A guide to convolution arithmetic for deep learning, arXiv preprint arXiv:1603.07285 (2016).
- [57] Conv2dtranspose layer, 2020. URL: https://keras.io/api/layers/convolution_layers/convolution2d_transpose/.
- [58] I. M. Sobol, Global sensitivity indices for nonlinear mathematical models and their monte carlo estimates, *Mathematics and computers in simulation* 55 (2001) 271–280.

- [59] A. Saltelli, M. Ratto, T. Andres, F. Campolongo, J. Cariboni, D. Gatelli, M. Saisana, S. Tarantola, Global sensitivity analysis: the primer, John Wiley & Sons, 2008.
- [60] R. Caflisch, Monte carlo and quasi-monte carlo methods, *Acta Numerica* 7 (1998) 1–49.